Injectable versatile liquid-solid transformation implants alliance checkpoint blockade for magnetothermal dynamic-immunotherapy

Mengna Wang [a,c], Siyu Deng [a], Yijia Cao [b], Hang Zhou [c], Wei Wei [a], Kexiao Yu [d,**], Youde Cao [a,e,f,***], Bing Liang [a,e,f,*]

[a] Department of Pathology, College of Basic Medicine, Chongqing Medical University, Chongqing, 400016, PR China
[b] Department of Digestion, University-Town Hospital of Chongqing Medical University, Chongqing, 401331, PR China
[c] Institute of Ultrasound Imaging of Chongqing Medical University; The Second Affiliated Hospital of Chongqing Medical University, 76 Linjiang Road, Yuzhong District, Chongqing, 400010, PR China
[d] Department of Orthopedics, Chongqing Traditional Chinese Medicine Hospital, No. 6 Panxi Seventh Branch Road, Jiangbei District, Chongqing, 400021, PR China
[e] Molecular Medicine Diagnostic and Testing Center, Chongqing Medical University, 1 Yixueyuan Road, Yuzhong District, Chongqing, 400016, PR China
[f] Department of Pathology, the First Affiliated Hospital of Chongqing Medical University, 1 Youyi Road, Yuzhong District, Chongqing, 400042, PR China

ARTICLE INFO

ABSTRACT

The ongoing circulating energy loss, low reactive oxygen species (ROS) accumulation and poor immunogenicity of tumors make it difficult to induce sufficient immunogenic cell death (ICD) in the tumor immunosuppressive microenvironment (TIME), resulting in unsatisfactory immunotherapy efficacy. Furthermore, for highly malignant tumors, simply enhancing ICD is insufficient for exhaustively eliminating the tumor and inhibiting metastasis. Herein, we propose a unique magnetothermal-dynamic immunotherapy strategy based on liquid-solid transformation porous versatile implants (Fe_3O_4/AIPH@PLGA) that takes advantage of less energy loss and avoids ongoing circulating losses by minimally invasive injection into tumors. In addition, the magnetothermal effect regresses and eliminates tumors that are not limited by penetration to simultaneously trigger 2,2′-azobis[2-(2-imidazolin-2-yl) propane] dihydrochloride (AIPH) decomposition and generate a large amount of oxygen-irrelevant free radicals and heat shock protein (HSP) accumulation by heating, evoking both intracellular oxidative stress and endoplasmic reticulum (ER) stress to induce large-scale ICD and enhance tumor immunogenicity. More importantly, in orthotopic bilateral breast tumor models, a significant therapeutic effect was obtained after combining amplified ICD with CTLA4 checkpoint blockade. The 21-day primary and distant tumor inhibition rates reached 90%, and the underlying mechanism of the effective synergetic strategy of inducing the T-cell-related response, the immune memory effect and TIME reprogramming in vivo was verified by immune cell analyses. This remarkable therapeutic effect provides a new direction for antitumor immunotherapy based on magnetothermally controlled oxygen-independent free radical release.

1. Introduction

Cancer immunotherapy that activates the immune system to fight cancer can result in significant tumor regression [1,2]. Recently, it has been found that immunological checkpoint blockade (ICB) can impair the escape of tumor cells from the host immune system and facilitate the activation of immune effector cells by enhancing T-cell infiltration [3,4]. The initiation of checkpoint blockade with anti-PD-1, anti-PD-L1, or anti-cytotoxic T-lymphocyte-associated protein-4 (anti-CTLA-4) antibodies has shown promising clinical progress in the treatment of a range of malignancies [5,6]. Unfortunately, a majority of tumors are cold tumors with minimal immunogenicity, particularly highly malignant

tumors such as triple-negative breast cancer (TNBC) [7,8]. The tumor immunosuppressive microenvironment (TIME) in cold tumors makes it difficult to generate robust immune cell infiltration, giving rise to a limited antitumor immune effect [9,10]. As a result, there is an urgent need to investigate realistic techniques for activating antitumor immunity while also converting cold tumors into hot tumors.

Emerging free radical-based therapy has been discovered to be an effective strategy for triggering tumor cell death and increasing the response rate of checkpoint blockade therapy by overcoming the TIME [11,12]. However, the therapeutic effectiveness of these free radical-based anticancer methods is extremely oxygen-dependent and is significantly restricted by the hypoxic tumor microenvironment. Moreover, endogenous ROS are transient species with a short half-life (10–320 ns), and show narrow dispersion range (10–55 nm), and limited accumulation, leading to low immunogenic cell death (ICD) efficacy [13,14]. Recently, oxygen-irrelevant thermal dynamic therapy was proposed for hypoxic tumor therapy, in which 2,2′-azobis[2-(2-imidazoline-2-yl)propane] dihydrochloride (AIPH), a heat-labile molecule that decomposes rapidly and releases free radicals under heat stimulation without oxygen dependence, was used as a thermally activated free radical generator [15,16]. These nanoplatforms can be transported to tumor sites and produce free radicals under thermal stimuli [14,17,18].

Magnetic-thermal therapy (MTT) is a minimally invasive tumor ablation method that utilizes the heat generated from a magnetic medium under an alternating magnetic field (AMF) to locally ablate tumors [19,20]. Compared to photothermal dynamic therapy for the release of free radicals and ablation of tumors by photonic irradiation, magnetic-thermal dynamic therapy (MDT) is a promising therapeutic method for overcoming the therapeutic depth limitations of photothermal therapy, allowing MDT to be combined with immunotherapy for improved efficacy in combating tumors [19,21]. To this end, several oxygen-independent therapeutic platforms enabled by nanotechnology have been reported [15,22]. Although classic magnetic Fe_3O_4 nanoparticles have been employed effectively for in situ localized tumor eradication, the nonspecific distribution of Fe_3O_4 nanoparticles in vivo could result in additional side effects [23]. Moreover, it is difficult to implant large magnetic particles and magnetic seeds into tumor tissues in situ due to some side effects, and the elimination of large particles from the body is also difficult. In addition, the traditional medium of MTT, such as magnetic seeds, magnetic fluid and Fe_3O_4 nanoparticles, easily collapses in situ or is removed from the circulation, leading to lower energy conversion efficiency. Liquid-to-solid phase transformation materials have been recognized as suitable in situ implantable materials for magnetic-thermal therapy. These materials are injectable in their liquid phase so that they can be introduced into the tumor tissues in a minimally invasive manner, after which they could be rapidly in situ transformed into solid magnetic implants [24,25]. The produced solids can be easily controlled in vitro under an alternating magnetic field to produce therapeutic heat for initiating magnetic-thermal and free radical-based therapy. Moreover, liquid-to-solid phase-transitional materials can easily incorporate multiple hydrophobic, hydrophilic drugs and nanomedicines for advanced therapeutics that are advantageous for combinational cancer treatment [19].

To improve the immunogenicity of cancer cells, it is necessary to develop immunotherapy-involved combination strategies that may activate the immature dendritic cell (DC) maturation, and enhance the ability of mature DCs to recognize and capture tumor antigens [26]. ICD-related immunotherapy based on thermal effects or reactive oxygen species (ROS) toxicity has been used in the clinical application [9]. ROS regulate intracellular redox metabolism that involves highly reactive molecules or molecular fragments, and excessive oxidative stress further disrupts endoplasmic reticulum (ER) homeostasis by activating complex signaling pathways and causing ER stress, eventually enhancing ICD [27]. Many studies have shown that thermal therapy effectively kills tumors and leads to tumor cell death in an immunogenic manner [20]. However, these strategies have several shortcomings that have led to

suboptimal curative effects. A single hyperthermia treatment modality cannot completely cure tumors due to recurrence and distal metastasis [28]. More importantly, many anticancer therapies trigger the upregulation of adaptive immune checkpoints (ICs), such as PD-L1 or CTLA4, to some extent and tumor cells can be camouflaged to evade host immune surveillance, resulting in a lower response rate to antitumor therapies [29,30]. Moreover, we noticed that immune checkpoint blockade (ICB) prevents the immune escape of cancer cells, improving the anticancer immune response when used in combination with other treatments [31]. For malignant tumors such as TNBC, it is therefore a rational choice to adopt multiple comprehensive therapies to improve the curative effect.

Herein, for the first time, by coencapsulation of magnetic Fe_3O_4 and AIPH with the clinically popular biocompatible/biodegradable organic macromolecule polylactic-coglycolic acid (PLGA) to form Fe_3O_4/AIPH@PLGA (denoted F/A@P), we obtained a unique type of injectable implant that can initiate MDT via a liquid-to-solid phase-transitional mechanism within tumor tissues. As constructed, Fe_3O_4/AIPH@PLGA was expected to show the following features. First, Fe_3O_4/AIPH@PLGA can be fabricated in the liquid phase in vitro and can serve as an injectable implant for in vivo applications. Fe_3O_4/AIPH@PLGA can swiftly diffuse into the surrounding aqueous environment after contacting the aqueous environment of tumor tissues. Hydrophobic PLGA then precipitates to produce a solid or semisolid implant that is confined to malignancies. Moreover, in-take of PLGA bypassed the circulation to escape the clearance effect of the liver and spleen. After phase transformation, the loaded Fe_3O_4 particle liquid gels become a solid implants without dispersion and strongly increase the magnetic-thermal energy conversion efficiency. Second, Fe_3O_4/AIPH@PLGA can perform MTT under an AMF and decompose AIPH for free radical-based oxygen-irrelevant MDT therapy. The MDT can combat tumors without deep limitations and noticeable thermal loss. Moreover, the MDT process can initiate ER stress and convert cold tumors into hot tumors to facilitate immunotherapy. More importantly, these synergetic effects magnify ICD and prompt dying cells to release sufficient immune signals as damage-associated molecular patterns (DAMPs). DAMPs improve the immunogenicity of cancer cells, assist with immature dendritic cell (DC) maturation, and enhance the ability of mature DCs to recognize and capture tumor antigens, thus stimulating the activation, proliferation and infiltration of T cells in the TIME and eliciting a strong anticancer immune response. In combination with anti-CTLA-4 therapy, Fe_3O_4/AIPH@PLGA showed superb antitumor performance for both primary tumors and distant tumors. In addition, the liquid-to-solid phase-transition Fe_3O_4/AIPH@PLGA does not damage normal tissues, indicating high biocompatibility (Scheme 1). Thus, our study engineered unique oxygen-irrelevant free radical-generating hydrogels in which Fe_3O_4/AIPH@PLGA can act as magnetic materials for in situ robust magneto-thermal dynamic-immunotherapy.

2. Experimental section

2.1. Materials

PLGA (lactide/glycolide = 50:50) was obtained from Jinan Daigang Biomaterial Co. (China). NMP was obtained from Aladdin (China). Fe_3O_4 NPs were purchased from Chengdu Aike Reagent (China). AIPH was purchased from Adamas beta (China). All of the chemicals used in this work were of analytical grade and were kept reasonably according to the manufacturer's instructions. The anti-CTLA4 antibody applied in vivo was obtained from Bioxcell (USA). Antibodies against cell surface markers for the FCM assay were acquired from BioLegend, eBioscience (USA). Antibodies against CRT, HMGB1, HSP70, and HSP90 were purchased from Abcam (USA). ELISA kits for IL-12, IL-6, TNF-α and IFN-γ were obtained from Quanzhou Jiubang Biotechnology Co. (China). A fluorescent cell imager (ZOE Fluorescent Cell) was purchased from Bio-Rad (USA). Bio-TEM images were acquired from Hitachi-7800 machine (Japan).
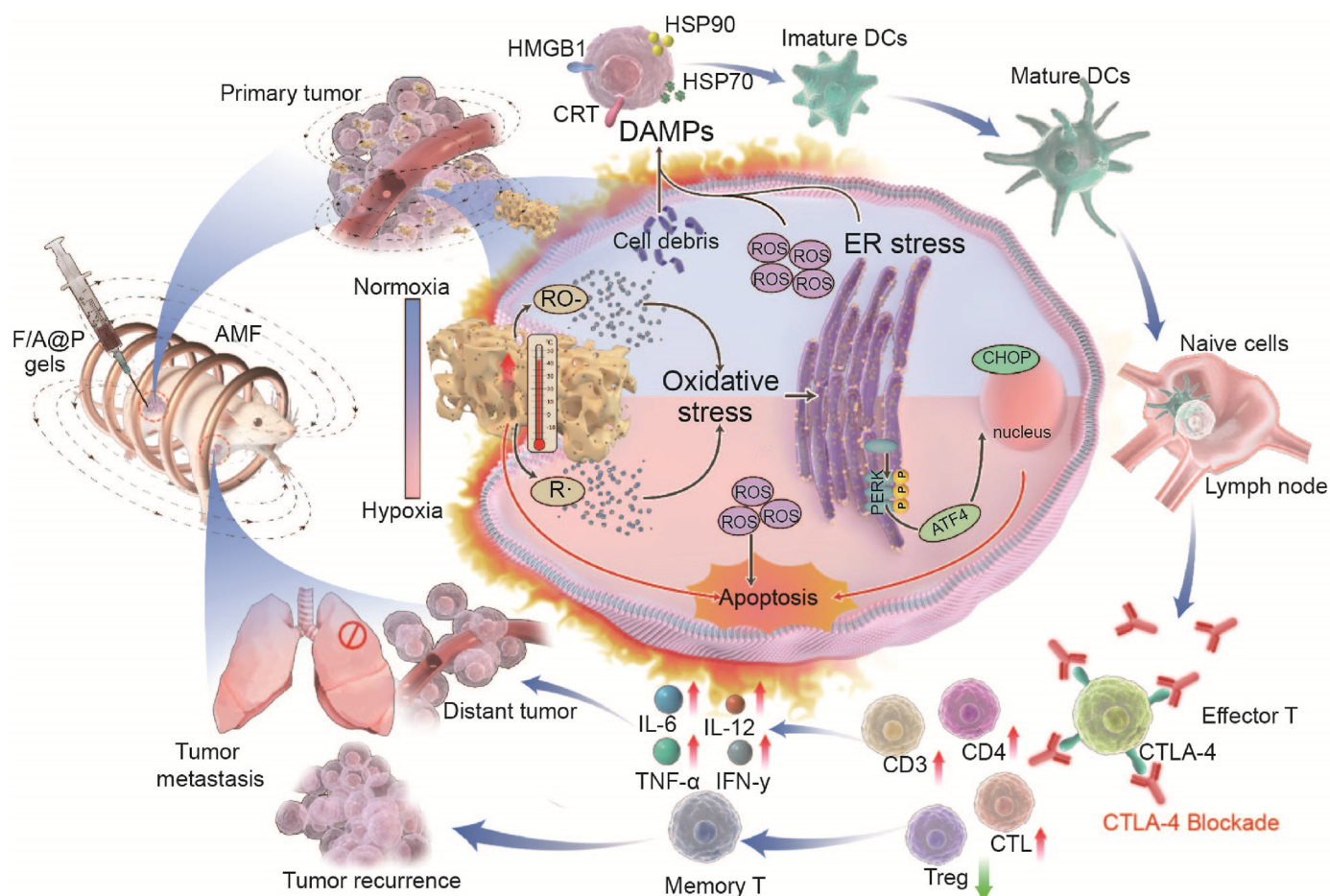
Scheme 1. Scheme of F/A@P gel-mediated augmented anti-TNBC immunotherapy: the magnetothermal effect with ROS dual-induced ICD effective reversal of poor tumor immunogenicity combined with ICB blockade to enhance TNBC immunotherapy efficacy.

2.2. Synthesis and characterization of the F@P and F/A@P hydrogels

PLGA and NMP were mixed at a fixed PLGA/NMP ratio of 0.5–0.6 and stirred in a shaker at 37 °C for 48 h until they were completely dissolved to obtain PLGA hydrogels. As shown in Table 1, Fe_3O_4 and AIPH were dispersed into PLGA hydrogels at different mass ratios to synthesize the F@P and F/A@P hydrogels. To obtain cross-sections of the PLGA and F/A@P hydrogels, the materials were quickly frozen under liquid nitrogen and brittle fracture conditions. The morphologies of the Fe_3O_4 and AIPH particles and PLGA and F/A@P hydrogels were analyzed by SEM (ZEISS GeminiSEM 300, Germany), and the elements were qualitatively analyzed by energy-dispersive X-ray spectroscopy (EDS). The infrared spectra of the PLGA, Fe_3O_4, AIPH, F@P and F/A@P hydrogels were recorded using an FTIR spectrometer (Nicolet 6700). XRD experiments were carried out with a Rigaku Ultima IV (Japan). XPS measurements were performed using a Thermo Scientific K-Alpha instrument. Hysteresis loop analysis was carried out with a Lakeshore 7404 instrument. The amounts of the inorganic components incorporated in the PLGA and F/A@P hydrogels were determined by TGA (TGA5500). UV–vis–NIR absorption spectra were acquired with a UV-3101PC Shimadzu spectrometer. The pore structures of the prepared hydrogels were observed with an automatic pore analyzer (AutoPore 9500). The ICP-OES/MS results of the prepared hydrogels were obtained using an Agilent 5110(OES) instrument (Agilent USA). The AMF generator (coil turn: 2, coil length: 1 cm, coil diameter: 3 cm, frequency: 626 kHz, output current: 28.6 A, field strength: 5.72 K/Am) was used as the radiation source to trigger the magnetothermal effect.

2.3. AIPH release

The maximum ultraviolet absorption peak of AIPH is located at 225 nm. The prepared 75 μL F/A@P gel was placed in a 15 mL centrifuge tube, PBS (10 mL) was added, and the mixture was exposed to AMF for 400 s. At 24 h, the supernatant was taken for UV determination. The retrieved hydrogels were harvested and then homogenized by NMP solvent (1 mL) to release the residual AIPH for 24 h. After homogenization, the samples were centrifuged at $10,000 \times g$ for 10 min, and the supernatant was used for ultraviolet analysis determination.

2.4. Cell culture

4T1 breast tumor cells were purchased from Procell (Wuhan, China), cultured in complete DMEM and grown in an atmosphere composed of 5% carbon dioxide (CO_2) and 95% air at 37 °C.

Table 1
Composition of F@P and F/A@P hydrogels.

Immune Gels	Powder (mg)		PLGA hydrogels (mL)
	Fe_3O_4	AIPH	
F@P	91.95	0	1
F\A@P-4% Fe_3O_4	43.95	54.47	1
F\A@P-8% Fe_3O_4	91.95	54.94	1
F\A@P-12% Fe_3O_4	144.57	60.24	1

2.5. In vitro magnetothermal effect of F/A@P

To evaluate the magnetothermal performance of F/A@P, varying mass ratios of Fe_3O_4 NPs (4%, 8% and 12%) and different volumes of F/A@P (50 μL, 75 μL, and 100 μL) were placed into a freshly isolated bovine liver and PBS in Eppendorf tubes. The magnetothermal properties of F/A@P under AMF actuation were determined using a far-infrared thermometer (FOTRIC225, ZXF Laboratories, USA), and temperature changes from thermal images were analyzed using the AnalyzIR 7.1 software. All of the above experiments were carried out in triplicate in each group.

2.6. In vitro therapeutic efficacy of F/A@P

4T1 cells were inoculated into 96-well plates at a density of 1×10^4 cells per well and treated with various treatments for 24 h and 48 h. Cell viability was then determined by CCK8 assay. 4T1 cells were inoculated into 35 mm glass-bottom dishes (1×10^5 cells per dish). Then, the cells treated with different treatments for 24 h and washed with PBS three times. Then, Calcein-AM (15 μL) and PI (5 μL) were added to the dishes to stain living (green) and dead (red) cells. After 15 min of staining, the cells were washed three times with PBS and observed with a fluorescent cell imager. Additionally, 4T1 cells were inoculated into 6-well plates at a density of 4×10^5 per well after different treatments for 24 h. The cells were then washed three times with PBS, harvested by trypsinization and centrifuged at 2000 rpm for 5 min. The cells were resuspended in PBS, and then Annexin V-FITC (5 μL) and PI (10 μL) were added for 20 min of incubation before performing FCM analysis.

2.7. Generation of free radicals

To monitor free radical generation upon AMF actuation, a TMB aqueous solution and F/A@P (75 μL) were added to a tube and then exposed to an AMF. The absorbance of each solution was recorded with a UV–vis–NIR spectrophotometer. 4T1 cells were treated with different treatments at 37 °C for 24 h, and DCFH-DA was used as the fluorescent probe to monitor intracellular free radical generation. After staining with DCFH for 30 min, the fluorescence of the activated DCF was measured with a fluorescent cell imager. Using the approach described above, DCFH-stained 4T1 cells were collected, and FCM was used for detection.

2.8. In vitro GSH depletion

4T1 cells were treated with different treatments at 37 °C for 24 h. PBS-treated cells were used as the control. Then, the intracellular GSH level was determined based on the kit instructions. The relative GSH level in each treatment group was calculated based on the control group.

2.9. In vitro ER stress analysis by western blot

4T1 cells were inoculated in six-well plates and treated differently at 37 °C for 24 h. Then, the cells were collected, and cellular protein was extracted. PERK, pPERK, ATF4, and CHOP antibodies were used to detect the corresponding protein expression levels by electrophoresis.

2.10. In vitro ICD effect

The expression levels of HMGB1, CRT, HSP70 and HSP90 were detected by cellular immunofluorescence to evaluate ICD. 4T1 cells were exposed to various treatments at 37 °C for 24 h. Then, the cells were incubated with fixing liquid for 10 min. An anti-HMGB1 antibody was used to stain the cells for 30 min. Subsequently, the cells were washed three times with PBS and stained with FITC-IgG secondary antibody for 30 min. Finally, the cells were stained with DAPI for 15 min and washed three times with PBS. Anti-CRT, anti-HSP70, and anti-HSP90 antibodies were used with the same approach to stain treated 4T1 cells. All fluorescence images were acquired using a ZOE fluorescent cell imager.

2.11. In vitro DC maturation

DCs were isolated from the bone marrow of 8-week-old BALB/c mice. After various treatments, the 4T1 cell residues were cocultured with DCs for 24 h using a transwell system. Then, DCs were collected and stained with anti-CD11c-FITC, anti-CD86-APC and anti-CD80-PE and finally were sorted by FCM.

2.12. In vivo experiment

Female BALB/c mice (6–8 weeks) were purchased from Chongqing Medical University and all in vivo experiments were approved by the Animal Experimentation Ethics Committee of The First Affiliated Hospital of Chongqing Medical University. A bilateral 4T1 tumor model was established to investigate the therapeutic efficacy of magnetothermal immunotherapy. The day of the right mammary fat pad injection was defined as day −7, and the day of the injection on the left side was regarded as day −4. On day 0, the mice were randomly divided into 5 groups: (1) control, (2) F@P +AMF, (3) F/A@P+AMF, (4) F/A@P +anti-CTLA4, and (5) F/A@P +AMF+anti-CTLA4. In the appropriate groups, F/A@P and F@P were i.t. injected into the primary tumors and exposed to AMF the next day. Anti-CTLA4 antibody (clone 9H10, 20 μg per mouse) was injected intraperitoneally into the mice on the 1st, 3rd and 6th days. The tumor volumes and body weights of the tumor-bearing mice were monitored every 2 days for the whole treatment cycle. Tumor volume was calculated by the following formula: volume = width^2 × length/2. The mice were subjected to survival analysis and observed until day 40. Mice were euthanized when the tumor volume reached 1500 mm^3. The lung tissue was removed after the mice died and was fixed and stained with Bouin's fluid to observe the lung metastasis of the mice in each group.

2.13. In vivo analysis of immune activation

The lymph nodes (LNs), spleens and tumors of the mice were harvested to study the immune activation level. The LNs, spleens and tumor tissues were chopped and placed in a glass tube containing PBS (pH 7.4) and 2% heat-inactivated fetal bovine serum. Then, a single-cell suspension was prepared with a homogenizer under mild pressure without the addition of digestive enzymes. Finally, after the red blood cells (RBCs) were removed with RBC lysis buffer, the cells were stained with fluorescently labeled antibodies. According to the standard protocol, the spleen single-cell suspension was stained with anti-CD11C FITC, anti-CD86 APC, and anti-CD80 PE to assess DC maturity. Effector memory T cells (T_{EM} cells) were analyzed by spleen single-cell suspension staining with anti-CD3-FITC, anti-CD8-PE, anti-CD62 L Percp-Cy5.5 and anti-CD44-APC antibodies. Single-cell suspensions from the secondary tumors and spleens were further stained with anti-CD3-FITC, anti-CD4-APC, anti-CD8-PE, and anti-Foxp3 Percp-Cy5.5 antibodies to analyze the proportions of CTLs ($CD3^+CD4-CD8^+$), helper Th cells ($CD3^+CD4^+CD8-$), Teff cells ($CD3^+CD4+Foxp3-$), and Tregs ($CD3^+CD4+Foxp3+$). All of the antibodies used in our experiment were diluted 250-fold, and all samples were sorted and analyzed by FCM after staining.

2.14. Cytokine detection

The supernatants of the DC cell culture and mouse serum were collected. The levels of TNF-α, IFN-γ, IL-12 and IL-6 in the samples were analyzed by the corresponding ELISA kits.

2.15. In vivo synergistic therapy of tumors

After the treatment ended, the primary and distant tumors were collected from the mice. Liquid nitrogen was used to grind primary tumor, and total protein was extracted from tissue. Western Blotting analysis was performed to detected HSP70 levels in the primary tumors. The primary tumors were stained with H&E, Ki-67 antibody and TUNEL for histological analysis. Distant tumors were stained with CD8$^+$ immunochemical stain.

2.16. In vivo biosafety

Eight-week-old healthy BALB/c mice were randomly divided into 5 groups (n = 3 for each group). The noninjected group was used as a control, and F/A@P was injected on days 1, 7, 14, and 21 in the other 4 treatment groups. Serum and blood were collected, and biochemical and blood analyses were carried out using an automatic biochemical analyzer (Rayto, Chemray 240, China) and an automatic hematology analyzer (Mindray, BC-2800 VET, China). The main organs (lungs, heart, liver, spleen and kidney) of the mice were stained with H&E.

2.17. Statistical analysis

The data obtained in this work were analyzed using the GraphPad Prism 8.0 software. The values are shown as the means $\pm$ standard deviations (SDs). One-way ANOVA and Student's t-test were used for intergroup comparisons. Statistical significance: *$p < 0.05$, **$p < 0.01$, ***$p < 0.001$, and #$p < 0.05$, ##$p < 0.01$, ###$p < 0.001$.

3. Results and discussion

3.1. Synthesis and characteristics of F/A@P

Poly(lactic-co-glycolic acid) (PLGA) was approved by the US Food and Drug Administration (FDA) and can be used in medical biotechnology as an attractive material for clinical applications [24]. Based on our previous research, PLGA was dissolved into NMP solution and chemically polymerized, and Fe$_3$O$_4$ and AIPH were added for further, superior modification [32]. Hydrophobic PLGA was dissolved in N-methyl-2-pyrrolidone (NMP) to generate a homogeneous PLGA/NMP solution (PLGA hydrogel). Then, the reddish brown F/A@P hydrogel was easily synthesized by adding Fe$_3$O$_4$ and AIPH particles to the light yellow PLGA hydrogel (Fig. S1). The procedure for the synthesis of F/A@P is illustrated in Fig. 1a in the design of a minimally invasive strategy for treating TNBC, atraumatic implantation is the core problem. To show the high syringe suitability and fluidity of the as-prepared F/A@P gel bioinjection, the liquid form was inhaled into a standard syringe. It was found that F/A@P gels could freely pass through the syringe due to the low viscosity of the NMP solvent (Fig. 2b and Video-S1). Due to the fast solvent exchange between NMP and water, the phase transformation occurred immediately after contact with the water and the gel transformed to a solid form that was be easily removed from the water bath (Fig. 2b). This superb liquid-solid phase transformation property endows F/A@P gels with the ability of noninvasive injection into tumors, avoiding the possible disadvantages of the use of implant magnetic seeds during surgery.

Supplementary video related to this article can be found at https://doi.org/10.1016/j.mtbio.2022.100442.

To validate the successful formation of a suitable hydrogel structure, we characterized the obtained materials by scanning electron microscopy (SEM). As shown in Figs. S2-4, PLGA had a porous and loose structure, with an Fe$_3$O$_4$ nanoparticle (NP) size of 125.60 $\pm$ 37.85 nm, and that of AIPH was 19 $\pm$ 12.36 μm. SEM images of the F/A@P hydrogels showed a sponge-like morphology that is due to the loose and porous structure of PLGA. The Fe$_3$O$_4$ particles and rod-shaped AIPH were densely distributed and coated by PLGA (Fig. 1c). After AMF actuation, an average pore diameter increase of 2.56 $\pm$ 0.82-fold compared to F/A@P was observed that was mainly due to the thermal effect generated by the heating process that promoted solution exchange and gave rise to the solid-phase PLGA porosity. The porous sponge-like structure provides the space necessary for AIPH decomposition to effectively release free radicals into the surrounding tissues. The major elements (C, Fe, O, N, and Cl) were uniformly distributed as observed in the elemental mapping images, in agreement with the line scan energy spectrum analysis results shown in Fig. 1d. In addition, the Fourier transform infrared (FTIR) spectrum of F/A@P showed a characteristic absorption peak of AIPH at 1600 cm^{-1}, demonstrating its presence (Fig. 1e); the AIPH was uniformly distributed in the F/A@P gels. The natural structure of F/A@P was explored using X-ray diffraction (XRD), with the obtained results corresponding to the standard data for Fe$_3$O$_4$ (PDF#40-1120) (Fig. 1f). The elemental composition of F/A@P was further investigated by X-ray photoelectron spectroscopy (XPS). The spectrum of F/A@P exhibited the characteristic peaks of C, Fe, O, N and Cl (Fig. 1g), and the valence states of the elements did not change, demonstrating the successful synthesis of the F/A@P hydrogels and the stability of the procedure.

The drug loading rate of Fe in the F/A@P hydrogel was 5.39% as measured by ICP, and the encapsulation rate of Fe was 97.13%. Meanwhile, the drug loading rate of AIPH in the F/A@P hydrogel was 4.57% by ultraviolet determination and the encapsulation rate of AIPH was 95.65%. To enable MTT, F/A@P must show good magnetic performance. At 300 K (26.85 °C), the hysteresis loops (Fig. 1h) of the F/A@P and Fe$_3$O$_4$ NPs were narrow, showing their soft magnetic performance, and their corresponding saturation magnetization values were 0.35 emu/g and 3.08 emu/g, respectively. For these soft magnetic materials, the correlation between the low coercive field and hysteresis loss properties further demonstrated that F/A@P can be heated by AMF. As a sponge-like implant material with abundant pores, the F/A@P hydrogel can effectively release small molecular compounds or drugs. According to Figs. S5-7, the F/A@P gel was driven by AMF for 400 s, with 89.19% release of AIPH in 24 h. Thermogravimetric analysis (TGA) of F@P and F/A@P was performed by heating from 30 °C to 800 °C. Compared with F@P, the weight loss of the as-prepared F/A@P was 12.5%, which was attributed to thermolysis of the loaded AIPH small molecules (Fig. 1i), illustrating that AIPH has thermal decomposition ability. Collectively, the AIPH and Fe$_3$O$_4$ particles were uniformly distributed into the PLGA gels, and the successfully synthesized F/A@P gels show phase change behavior and can be precisely injected in situ. The pore diameters of the gels can be increased by AMF actuation to assist with AIPH decomposition and free radical generation, providing the basis for the local treatment of TNBC.

3.2. Magnetothermal performance and therapeutic efficacy of F/A@P with various components in vitro

To achieve controllable ranges of thermal radiation and heating temperature in vivo, the magnetic hyperthermia performance of F/A@P needs to be accurately evaluated under AMF. As shown in Fig. S8, 9, F/A@P can effectively enhance its own temperature and that of the surrounding PBS due to the conversion of electromagnetic energy into thermal energy by the Fe$_3$O$_4$ NPs. To rationally select the component ratio of F/A@P for in vivo treatment, a bovine liver was used to evaluate and imitate the heating process in vitro. F/A@P hydrogels were injected into the excised bovine liver pieces. The thermal images (Fig. 2b) and corresponding temperature curves (Fig. 2a) of the bovine liver implanted with F/A@P illustrate that the magnetic hyperthermia efficiency increased proportionately with Fe$_3$O$_4$ quantity, F/A@P volume, and AMF actuation time. It was determined that 75 μL of 8% F/A@P was needed to reach a temperature of 43 $\pm$ 1.1 °C in 150 s (Fig. 2a). For 100 μL of 8% F/A@P and 75 μL of 12% F/A@P, the temperature increase was too fast to control and can result in the damage to and necrosis of the peripheral normal tissue. Moreover, the thermal behaviors of 50 μL of 8% F/A@P and 75 μL of 4% F/A@P were too mild to achieve a therapeutic effect;
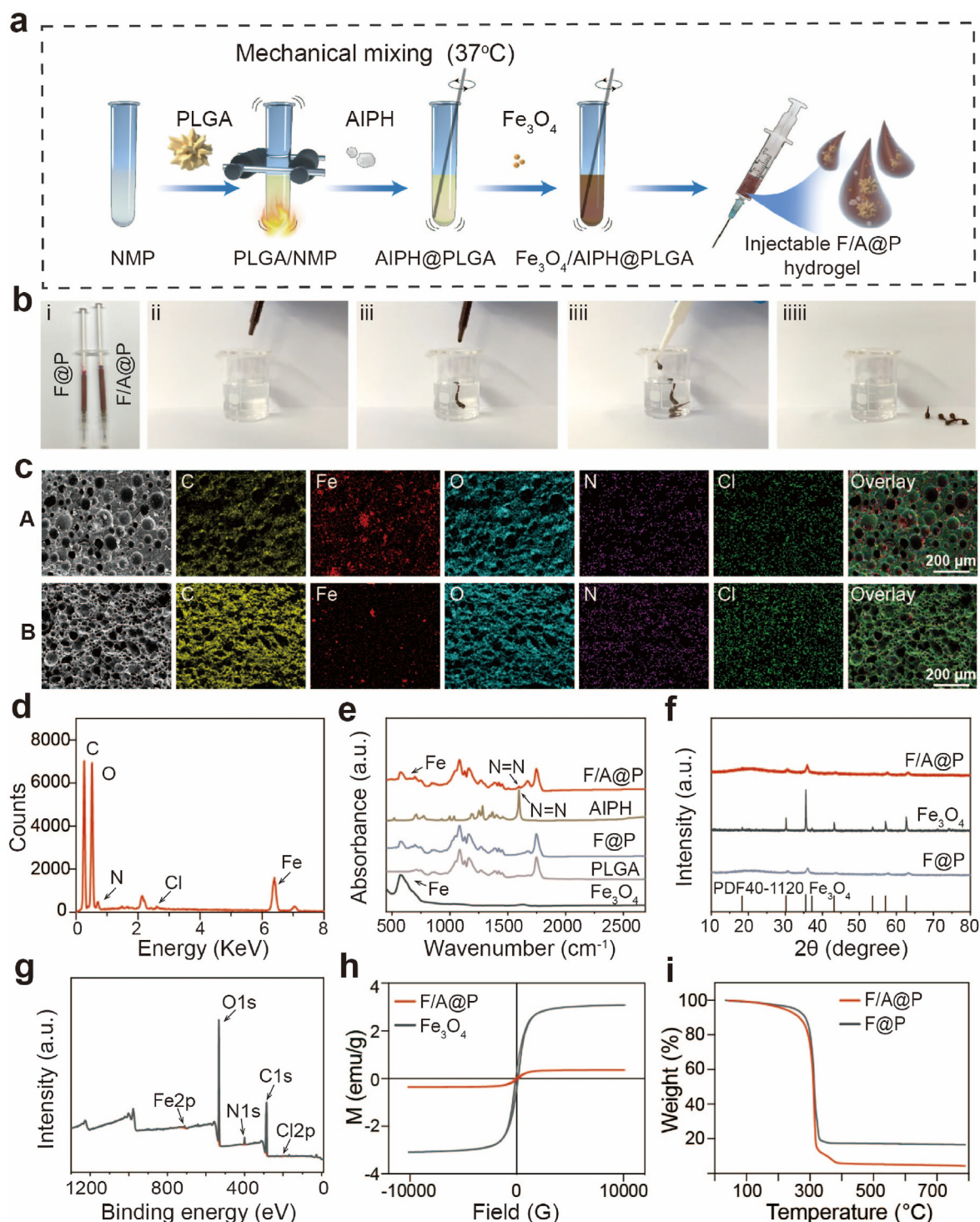
Fig. 1. Synthesis and characteristics of F/A@P. (a) Schematic diagram of the synthesis of F/A@P and F@P. (b) Digital photographs of the injectable F/A@P though the standard 1 mL syringe (i) and (ii-iiiii) the corresponding phase-change process after contacting the water. (c) SEM images of A) F/A@P and B) F/A@P + AMF and the corresponding elemental mapping images (scale bars: 200 μm). (d) Energy spectrum of F/A@P. (e) FTIR spectra of F/A@P, F@P, AIPH, PLGA, and Fe_3O_4. (f) XRD spectra of F/A@P, F@P, and Fe_3O_4. (g) XPS survey spectrum of F/A@P. (h) Magnetic hysteresis loops of F/A@P and Fe_3O_4. (i) TGA curves of F/A@P and F@P.

thus, their subsequent application in vivo was precluded. Temperatures in the range of 43–45 °C can not only eradicate cancer cells directly with little damage to surrounding normal tissue but also induce a systemic immune response [20]. As shown in Fig. 2c, 75 μL of 8% F/A@P was repeatedly exposed to AMF for seven on/off cycles, and no evident thermal attenuation was observed, demonstrating the high magneto-thermal stability of F/A@P during the thermal process. Consequently, 75 μL of 8% F/A@P was chosen in this work as the optimal MDT conditions

for triggering AIPH decomposition and stimulating the immune system, and is a rational choice for the subsequent cancer therapy and immunity activation applications.

After it was determined that the F/A@P free radical-generating gels have superb magnetothermal properties, their anticancer lethality was investigated, because this is another important property. F/A@P gels are highly biologically safe materials for intratumoral injection in situ and are nontoxic. As expected, almost no cytotoxicity was observed after
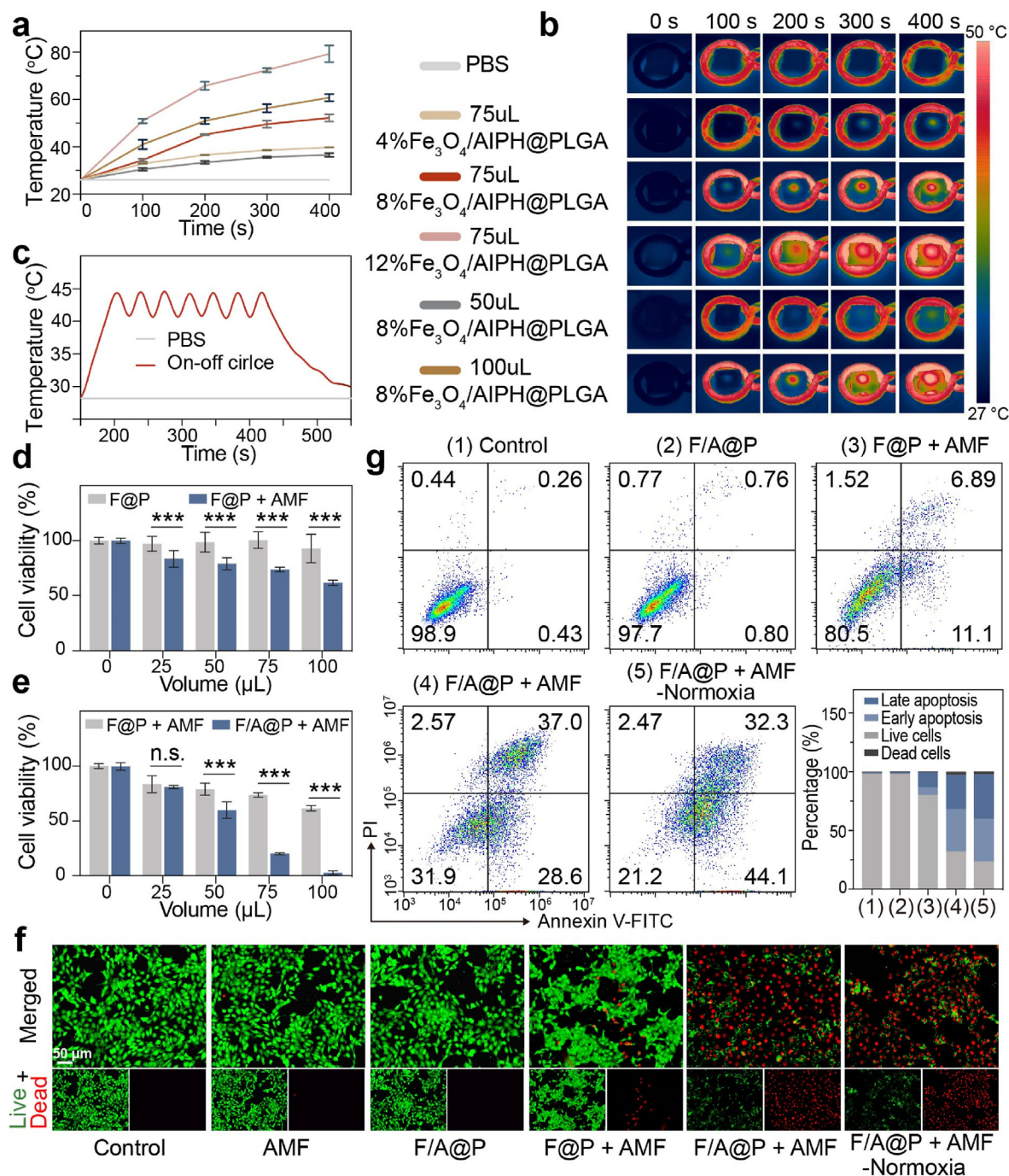
Fig. 2. Magnetothermal performance and therapeutic efficacy of F/A@P with various components in vitro. (a) Magnetothermal curves of different volumes and mass fractions of Fe_3O_4 in F/A@P under AMF actuation and (b) the corresponding infrared thermal images. (c) Temperature curves of F/A@P over seven on-off cycles under AMF actuation. (d–e) Viability of 4T1 cells after different treatments assessed by CCK8 assay. (f) Live (green)/dead (red) fluorescence images of 4T1 cells after different treatments (scale bars: 50 μm). (g) FCM was used to determine the apoptosis level of 4T1 cells after various treatments. The data are shown as the mean ± SD, n = 3 per group; *p < 0.05, **p < 0.01, ***p < 0.001.

treating 4T1 cells with various volumes of F/A@P for 24 and 48 h and F/A@P loaded with different percentages of AIPH for 24 h in the absence of AMF (Figs. S10 and 11). Moreover, the live/dead cell fluorescence signals were observed by confocal laser scanning microscopy (CLSM) (Fig. 2f), and a distinct green signal was detected in the groups treated with F/A@P alone and AMF actuation alone, illustrating the excellent biocompatibility of both F/A@P and AMF actuation. However, 4T1 cell viability declined with increasing volumes of F@P and F/A@P upon AMF actuation. When the gel volume was increased to 75 μL, the cell survival rate was approximately 20.1% ± 0.7 in the F/A@P + AMF group, which was

noticeably lower than that of 73.6% ± 1.8 for the F@P + AMF group under the same conditions (Fig. 2d and e). Therefore, due to the augmented anticancer efficacy exhibited in the 75 μL F/A@P group, this treatment was used in our following experiments. As shown in the fluorescence images (Fig. 2f), the F@P + AMF group displayed some red fluorescence, indicating that a single magnetothermal treatment can produce a limited cytotoxic effect. The evidenced red fluorescence signals were detected when 4T1 cells were incubated with F/A@P and subsequently exposed to AMF in both normoxic and hypoxic environments. Similar results were observed in the Annexin V-FITC/PI staining

assays (Fig. 2g), where an outstanding curative effect was observed in the F/A@P + AMF groups under normoxic and hypoxic conditions, both of which induced distinct cell apoptosis. These findings confirmed the necessity of blending AIPH as a free radical generator for tumor elimination, and such rapid generation of oxygen-independent free radicals triggered by the magnetothermal effect could efficiently accelerated cancer cell death.

3.3. Oxygen-irrelevant free radical generation ability of F/A@P and the mechanism of ER stress in vitro

Encouraged by the excellent therapeutic efficacy of F/A@P under AMF actuation in vitro, we used a free radical indicator, 3,3′,5,5′-tetramethyl benzidine (TMB), to validate the ability of F/A@P to generate free radicals. A typical absorption peak appeared at 652 nm when TMB was reacted with the generated free radicals. As displayed in Fig. 3a,-c, after the reaction between TMB and F/A@P under AMF actuation, the absorption peak gradually increased in a time-dependent manner; this was remarkably different from the results observed for the AIPH, F/A@P, and AIPH + AMF groups. Interestingly, the F/A@P + AMF group reached its peak absorption in the 100th second of heating. Moreover, we utilized a DCFH kit to evaluate the intracellular free radical-generating ability of F/A@P under AMF actuation in both normoxic and hypoxic conditions and compared these results with those obtained using the commonly
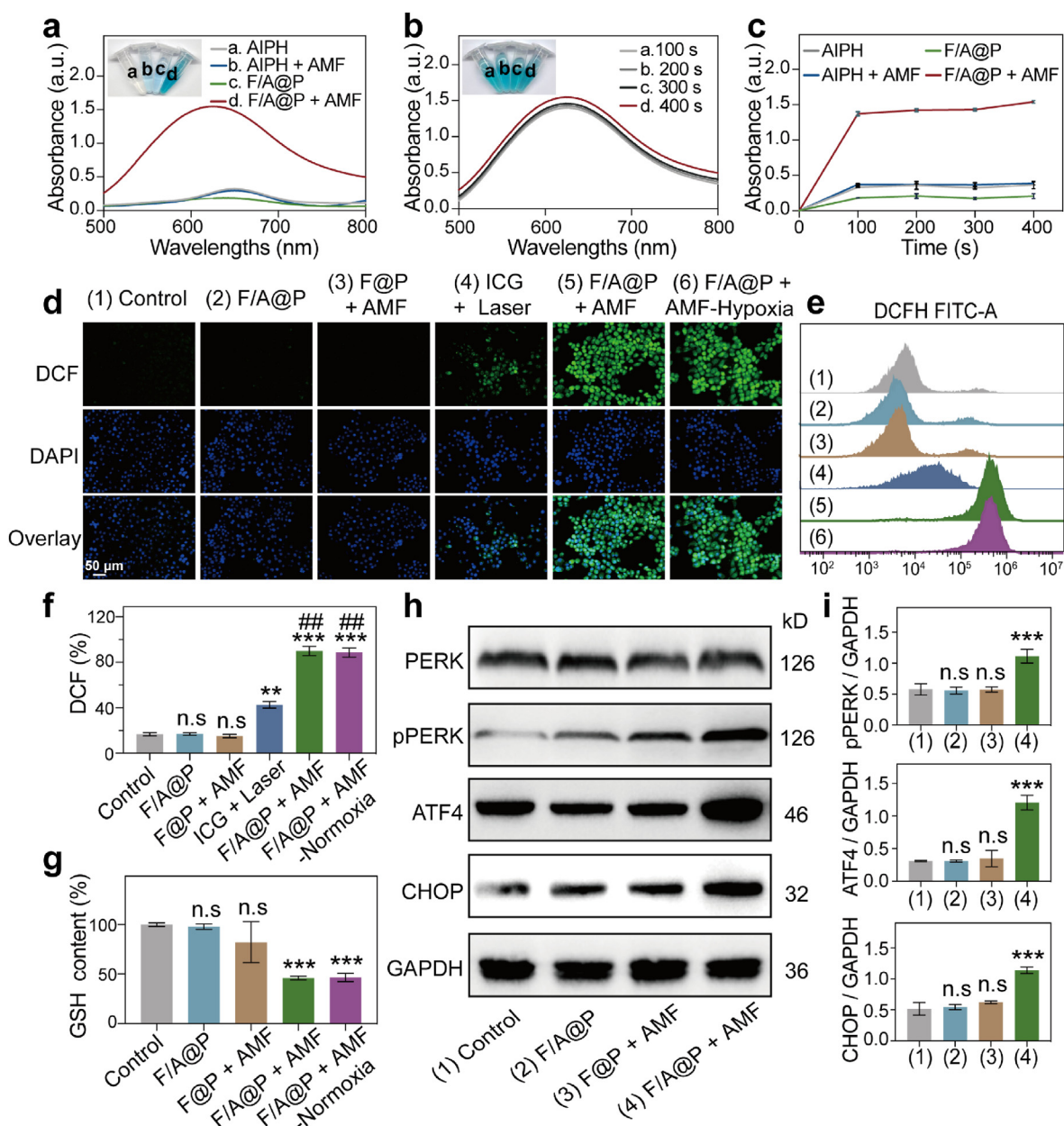

Fig. 3. Oxygen-irrelevant free radical-generating ability of F/A@P and the mechanism of ER stress in vitro. (a) UV–vis spectrum of oxidized TMB in different groups after AMF actuation for 400 s (inset: digital photos of the TMB solutions). (b) UV–vis spectrum of oxidized TMB after treatment with F/A@P under different AMF actuation times (inset: digital photos of the TMB solutions). (c) Absorbance curves of oxidized TMB based on a) and b). (d) Typical DCF fluorescence images of ROS levels in 4T1 cells after various treatments (scale bars: 50 μm). (e) Intracellular ROS levels after different treatments analyzed by FCM and (f) the corresponding quantitative analyses of ROS levels. (g) Intracellular GSH levels after different treatments. (h) Representative immunoblot results of various protein expression levels from each group. (i) Corresponding quantitative analyses of the ratios of p-PERK/GAPDH, ATF4/GAPDH and CHOP/GAPDH based on h). (The data are shown as the mean ± SD, n = 3 per group; n.s. represents no significance, *p < 0.05, **p < 0.01, ***p < 0.001 in comparison with the control group, ##p < 0.01 in comparison with the ICG + laser group).

used ICG photosensitizer that is highly capable of generating ROS [23]. As shown in Fig. 3d, when exposed to the same AMF conditions, a remarkably bright intracellular green fluorescence signal was observed in the 4T1 cells incubated with F/A@P under both normoxic and hypoxic conditions. A markedly different result of a negligible green fluorescence signal was observed for the control, F/A@P, and F@P +AMF treatment groups, indicating that no free radicals were generated. Encouragingly, compared with ICG under laser irradiation, F/A@P under AMF actuation resulted in the generation of far more intracellular alkyl free radicals. In addition, qualitative and quantitative FCM analyses proved the rich intracellular ROS generation (Fig. 3e and f). In the presence of F/A@P +AMF-normoxia and F/A@P+AMF-hypoxia, the fluorescence intensity of DCF showed a strong increase and was much greater than that in the ICG with laser irradiation group, demonstrating the generation of abundant ROS in these groups. Collectively, a large amount of intracellular oxygen-irrelevant ROS was generated by F/A@P under AMF actuation, displaying greater ROS production than the ICG photosensitizer. Despite the superb ability of F/A@P to generate free radicals, a large amount of intracellular reducing substances, such as GSH, will inhibit the oxidation level. Therefore, we investigated the capability of F/A@P to deplete GSH in the TIME. GSH levels in the control group remained high but were markedly reduced in the F/A@P+AMF groups under both normoxia and hypoxia, as shown in Fig. 3g. These results suggest that our F/A@P gels can efficiently consume GSH and further augment the therapeutic efficacy of ROS.

Many ROS-responsive hydrogels that release therapeutics into the tumor microenvironment (TME) in a controlled manner that contains abundant ROS [33,34]. The F/A@P hydrogel, as an alkyl-loaded platform, releases abundant alkyl free radicals in the tumor microenvironment after thermal triggering to resist tumors. To further reveal the mechanism of the lethal effect of the toxic free radicals produced by the F/A@P hydrogel at the cellular level, we used bio-TEM (Fig. S12). It is observed from the ultramicro cellular structure that F/A@P precisely affected tumor cells, giving rise to cell membrane destruction, organelle damage and nuclear membrane dissolution. Protein folding in the ER is a complicated process with multiple steps; under severe or persistent stress conditions, protein variation and disulfide bonds result in defective synthesis or decreased synthesis, causing unfolded or misfolded proteins to accumulates in the ER [22,27]. When the limit of the degradation system for the removal the wrong proteins is exceeded, ER homeostasis collapses, activating the endoplasmic reticulum kinase PERK to undergo homodimerization, and activating ER stress through autophosphorylation and downstream signaling pathways [35,36]. The classical phosphorylation pathway mediated by PERK (PERK-pPERK-ATF4-CHOP) is a widely accepted signaling pathway to understand the mechanism underlying induced ER stress, for example due to ultraviolet radiation, methotrexate and oxaliplatin [36,37]. Then, the damaged cells release DAMPs to the cell surface or extracellular fluid, thus inducing dendritic cells around the tumor cells to recognize specific antigens, arousing an immune response and improving the immunity of the body. These series of pathological processes make ER stress the general "initiator" factor of ICD events [35,37,38]. However, the mechanism of ER stress caused by alkyl free radical accumulation and the relationship with the ICD effect remain unclear. Herein, we speculate that F/A@P can cause tumor cells to enter a pathological state of redox damage by producing abundant free radicals. The accumulation of lipid oxidation and peroxidation, as well as the decrease in the reduced glutathione/oxidized glutathione (GSH/GSSH) ratio, increases the UPR load in the ER and leads to endoplasmic reticulum stress in tumor cells through the classical phosphorylation pathway mediated by PERK, eventually augmenting ICD scales in tumor cells. To verify the mechanism by which F/A@P induces ER stress, western blotting was used to investigate the PERK, pPERK, ATF4, and CHOP protein expression levels after treatment with F/A@P and AMF actuation. As shown in Fig. 3h, i, F/A@P + AMF upregulated pPERK (an indicator of the phosphorylation levels of PERK), and much higher protein expression levels of ATF4 and CHOP were detected

compared to those in the other groups. These comparison data demonstrate that F/A@P-mediated oxidative stress can upregulate the pathway of PERK-mediated phosphorylation that efficiently provokes ER stress, and ROS are the upstream event of endoplasmic reticulum stress. Taken together, these results show that the prepared F/A@P gels generated abundant oxygen-irrelevant free radicals and caused GSH depletion to increase oxidative stress and the pPERK pathway to evoke ER stress. This provides a mechanism premise for synergistically augmenting the scales of ICD.

3.4. F/A@P mediates immunogenic cell death and DC maturation in vitro

After verifying the mechanism by which F/A@P induces thermal effects and endogenous pressure in vitro, it is necessary to confirm whether F/A@P can trigger ICD. The characteristic biological event of ICD is the presence of activated DAMPs on the cell surface that act as activation signals for immune cells and reverse tumor cell immunogenicity, making cancer cells susceptible to immunotherapy [39,40]. We used cell immunofluorescence to assess the expression of the DAMP-related biomarkers HMGB1, CRT, HSP70, and HSP90 induced by F/A@P. As indicated in Fig. 4b, compared with the 4T1 cells in the PBS and F/A@P groups that exhibited almost no green fluorescence, the cells treated with F@P+AMF exhibited weak green fluorescence. By contrast, 4T1 cells treated with F/A@P+AMF exhibited significantly enhanced green fluorescence, suggesting elevated HMGB1 exposure on the 4T1 cell surface. Moreover, the green fluorescence of CRT, HSP70, and HSP90 in the F/A@P+AMF treatment group was also remarkably brighter than that for the other three groups. In marked contrast, almost no green fluorescence signal was detected in the control and F/A@P groups, indicating that no DAMP-related biomarkers were exposed in these groups. Overall, the DAMP-related biomarker fluorescence was notable in the F@P+AMF group, demonstrating that the thermal effect plays an important role in ICD. More importantly, the biomarker fluorescence in the F/A@P+AMF group was significantly brighter, indicating that ICD augmentation and immunogenicity enhancement can be induced by F/A@P under AMF actuation, which is related to the excellent F/A@P-mediated generation of free radicals. To conclude, both the thermal effect and endogenous stress mediated by F/A@P under AMF exposure have a synergistic effect on the induction of ICD.

DCs are extremely important for the activation of antitumor immune responses. It is important to note that the maturation state of DCs often determines the final result of T-cell activation that can secrete abundant stimulatory signals and contact T cells to evoke anticancer immunity [41, 42]. To investigate F/A@P-mediated DC maturation in vitro, BMDCs were cocultured with 4T1 cells in a transwell system as shown in Fig. 4a. DCs were collected, and the maturation ratios were determined by FCM. Upregulation of the costimulatory molecules CD80 and CD86 indicates the DC maturation level. As shown in Fig. 4c, the F/A@P group caused a negligible difference in DC maturation compared with the control group. The F@P +AMF group displayed a slight increase, but the DC maturation ratio in the F/A@P +AMF group reached 76.2% ±1.7, 4.7-fold higher than that in the control group, indicating the significant promotion of DC maturation. The release of tumor necrosis factor (TNF)-α, interleukin (IL)-6 and IL-12 in the F/A@P +AMF group was remarkably higher than that in the other groups, demonstrating that F/A@P under AMF actuation may stimulate the greatest immune responses in vitro (Fig. 4d). In summary, F/A@P hydrogels efficiently induced ICD by sufficient ecto-DAMP expression and activated DC maturation through intrinsic immune signaling, further improving antitumor immune responses in vitro.

3.5. Antitumor effect of F/A@P-mediated MDT combined with CTLA4 blockade therapy in an orthotopic 4T1 bilateral tumor-bearing mouse model

In view of the excellent antitumor effect, ICD induction and DC maturation produced by F/A@P in vitro, we further investigated the
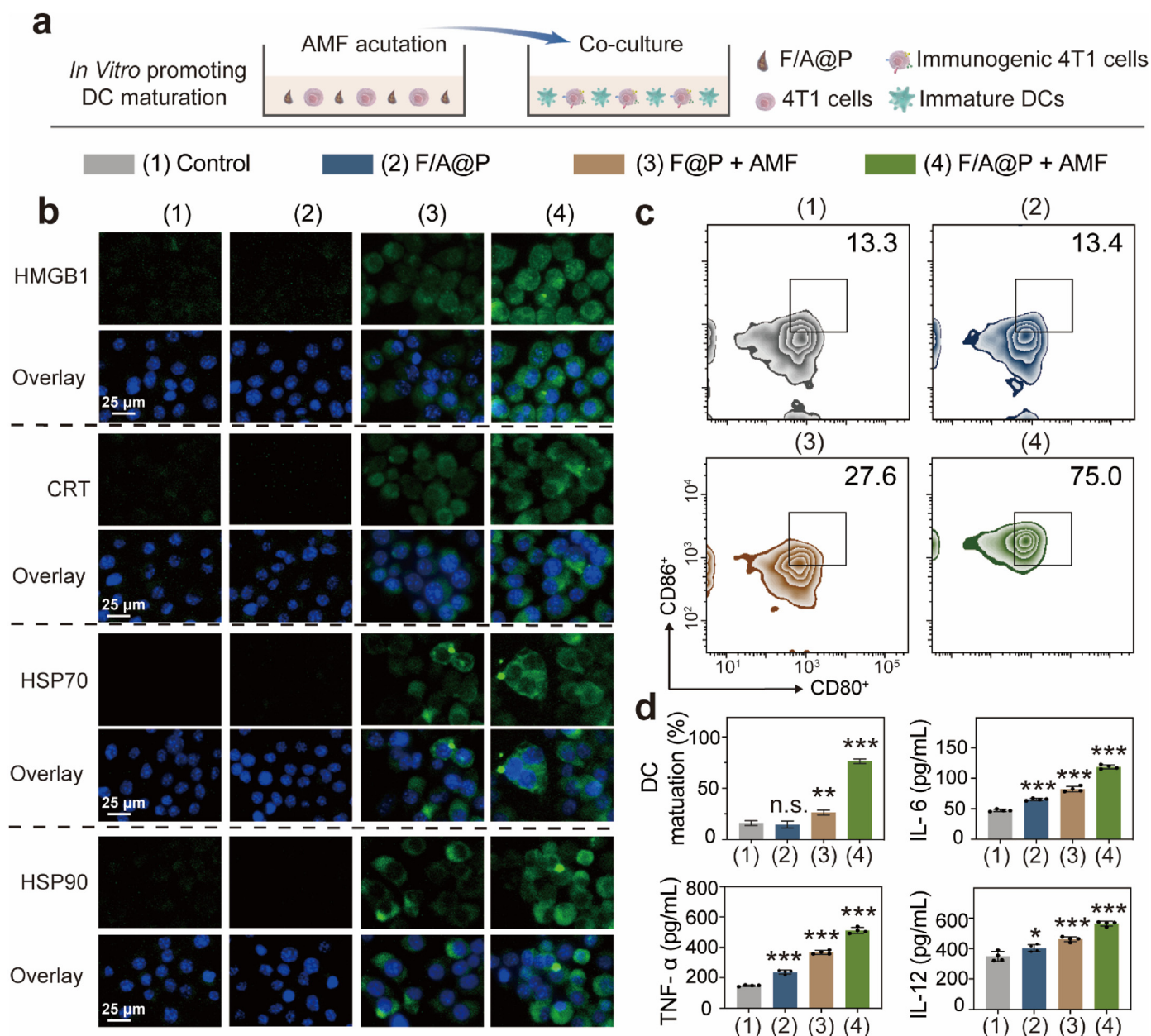
Fig. 4. F/A@P mediates immunogenic cell death and DC maturation in vitro. (a) Schematic diagram of the coculture process of immature DCs with 4T1 cell residues in vitro. (b) Immunofluorescence images of HMGB1, CRT, HSP70, and HSP90 expression in 4T1 cells (scale bars: 25 μm). Nuclei: blue, DAPI-labeled; specific cell surface proteins: green, FITC-IgG secondary antibody-stained. (c) The expression of CD80 and CD86 on the surface of the DCs in each group was analyzed by FCM. (d) Corresponding quantitative analysis of the DC maturation rates and levels of the cytokines IL-6, IL-12 and TNF-α in the supernatants of the DC culture medium. (The data are shown as the mean ± SD, n = 3 per group; n.s. represents no significance, *p < 0.05, **p < 0.01, ***p < 0.001 in comparison with the control group).

potential of F/A@P to be used as immune gels in breast-conserving treatments. Anti-CTLA4 has been approved by the FDA as an immune inhibitor and is currently applied in clinical practice. CTLA4 checkpoint blockade inhibits the camouflage and immune escape abilities of tumor cells by binding an anti-CTLA4 antibody to the CTLA4 receptor on T cells, blocking the activation of the inhibitory immune signal induced by anticancer therapy [43]. Many studies have confirmed that the effects of anti-CTLA4 are better than those of PD-L1 in inhibiting the activity of immunosuppressive regulatory T cells (Tregs) and improving immunotherapy efficacy [44]. CTLA4 blockade was introduced in our animal experiments to improve the immunotherapy efficacy of 'tumor vaccines' that are generated in situ following the F/A@P-mediated treatment of primary tumors. We established an orthotopic murine bilateral 4T1 (murine TNBC cells) breast tumor model with spontaneous metastasis,

and the therapeutic process is described in Fig. 5a. BALB/c mice were randomly divided into five groups, and the primary tumors were treated with PBS, F@P+AMF, F/A@P +AMF, F/A@P +anti-CTLA4, or F/A@P +AMF+anti-CTLA4. When the primary tumor volumes of the mice grew to 100–120 mm^3, the mice were i.t. injected with F@P or F/A@P and then exposed to an AMF. As shown in the infrared thermal images in Figs. S13 and 14, the temperature of the orthotopic breast tumors reached approximately 43 °C under AMF after intratumoral injection of F@P or F/A@P and remained between 43 and 45 °C for 6 min, indicating that mild MHT can be precisely achieved without notably damaging normal tissues based on AMF manipulation while simultaneously triggering AIPH decomposition in vivo.

The mouse tumor volume sizes were monitored, and photographs of the animals were taken after administration of the various treatments.
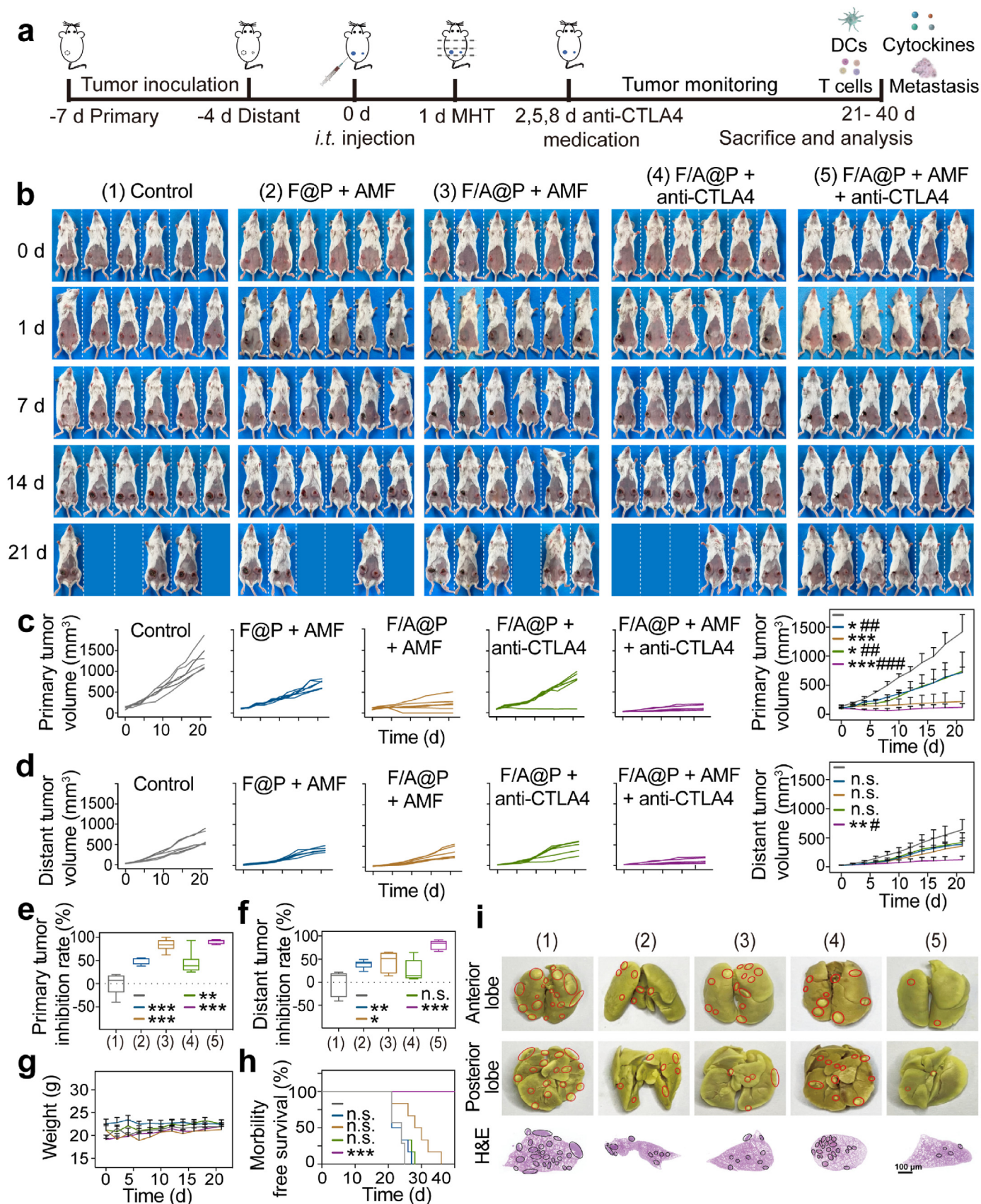
Fig. 5. Antitumor effect of F/A@P-mediated MDT combined with CTLA4 blockade therapy in an orthotopic 4T1 bilateral tumor-bearing mouse model. (a) Schematic diagram of F/A@P-mediated MHT combined with CTLA4 blockade therapy to inhibit primary and distant tumors. (b) Digital photographs of the mice in the five groups at 0, 1, 7, 14 and 21 days after various treatments. (c) Primary tumor growth curves and the average primary tumor growth curve of the mice in each group (n = 6). (d) Distant tumor growth curves and average distant growth curve of the mice in each group (n = 6). (e) Primary tumor inhibition rates and (f) distant tumor inhibition rates of the mice in each group. (g) Body weights and (h) morbidity-free survival of the mice in each group. (i) Digital photographs and H&E staining images of representative pulmonary metastatic nodules (circles) from the mice in each group at the end of treatment (scale bars: 100 μm). (The data are shown as the mean ± SD, n = 6 per group; n.s. represents no significance, *p < 0.05, **p < 0.01, ***p < 0.001 in comparison with the control group, #p < 0.05, ##p < 0.01, ###p < 0.001 in comparison with the F/A@P + AMF group).

Fig. 5b shows representative digital photographs of the mice in each group after the different treatments every 7 days. The treatment was carried out for 21 days. As illustrated in Fig. 5c, the primary tumor volume of the control group reached 1500 mm^3 on day 21, and the growth behaviors of primary tumors (n = 6) in the F@P+AMF and F/A@P +anti-CTLA4 groups appeared to be similar, while tumor growth in the F/A@P+AMF group was clearly inhibited. Significantly, the primary tumor of each mouse in the F/A@P+AMF+anti-CTLA4 group almost disappeared. Secondary tumor growth in the different groups is also recorded in Fig. 5d. For the mice in the control group, the secondary tumors showed quite rapid growth. Additionally, the secondary tumor growth rate was only mildly delayed if the mice were treated with F@P+AMF, F/A@P+AMF, or F/A@P+anti-CTLA4, all of which exhibited a similar trend. As treatment controls, the mild immunological responses induced by F@P+AMF (no free radical generation), F/A@P+anti-CTLA4 (no magnetothermal effect and no magnetothermal-responsive free radical generation) and F/A@P+AMF (no immune checkpoint blockade) suppressed the growth of the secondary tumors to only a certain extent. Excitingly, the best tumor treatment efficiency was observed after combination treatment with F/A@P+AMF plus anti-CTLA4. The primary tumors of these 4T1 model mice were eradicated and the growth of the secondary tumors was almost completely inhibited, showing significantly slowed tumor growth throughout the therapeutic cycle and demonstrating the important role of ROS toxicity, magnetothermal effects and anti-CTLA4 therapy to trigger effective antitumor efficacy and immune responses that are conducive to the treatment of tumor metastasis.

As displayed in Fig. 5e and f, the inhibition rates of both the primary and distant tumors were approximately 90% in the F/A@P+AMF+anti-CTLA4 groups, much higher than those in the other groups. There were no distinct differences in the body weights of the mice in all groups (Fig. 5g). The morbidity-free survival rate of the mice in the F/A@P+AMF+anti-CTLA4 group was also the highest compared with those for the other groups during 40 days of monitoring, demonstrating that this nonspecific immunotherapy procedure may be effective as a TNBC treatment (Fig. 5h). After the therapeutic regimens were finished, the efficacy of F/A@P to inhibit tumor metastasis was evaluated by examining the lung tumor nodules, as displayed in Fig. 5i. Digital photographs of Bouin liquid-stained whole lungs collected at the end of the therapeutic cycle displayed only a few signs of lung metastasis in the combination group with F/A@P-based MDT plus anti-CTLA4 therapy compared with the many nodules found in the other groups, and hematoxylin and eosin (H&E) staining showed the same results. Consequently, F/A@P exhibited high curative biosafety in vivo and can be used as an immune gel to not only eradicate primary tumors but also act as a source of an in situ 'tumor vaccine' combined with ICB to provide great potential for improving the efficacy of malignant tumor breast-conserving immunotherapy.

3.6. Immune response to combination therapy in an orthotopic bilateral 4T1 tumor-bearing mouse model

We further investigated antitumor immunity to explore the potential mechanism of the excellent efficacy and abscopal effect mediated by F/A@P in vivo. Thus, immune cells from LNs close to the primary tumors, spleens and distant tumors and cytokines from the serum were harvested and assessed. Immune cells were evaluated by FCM, and cytokines were evaluated by ELISA. Since F/A@P-mediated MHT and synergistic CTLA4 blockade can activate DC maturation that plays a critical role in antigen presentation and T-cell activation, DC maturation in the LNs and spleens was evaluated by FCM. Judging by the maturation ratio of DCs in LNs (≈40%) and spleens (≈50%) (Fig. 6a and b), the relative number of mature DCs increased remarkably after treatment with F/A@P+AMF+anti-CTLA4 and was notably higher than that in the PBS group, which may be due to both intrinsic immunomodulatory properties and magnetothermal effects. This result indicates the superior immuno-modulatory effect of F/A@P on the transfer of immature DCs to a mature antitumor phenotype.

Many studies have documented that helper T cells (Th cells; CD3$^+$CD4$^+$CD8-) are primarily responsible for regulating adaptive immunity, while CTLs (CD3$^+$CD4-CD8$^+$) eliminate targeted cancer cells directly [45,46]. Marked by Foxp3, CD4$^+$ Th cells can be classified as Tregs (CD3$^+$CD4+Foxp3+) that can inhibit antitumor immune responses, and effector T cells (Teff cells, CD3$^+$CD4+Foxp3-) that enhance antitumor immune effects [47]. As displayed in Fig. 6c, d, e, f, in the mice whose primary tumors were treated with F/A@P+AMF and F@P +AMF, there was mainly immunosuppressive Tregs were found in the spleens and distant tumors. Hence, although the immune system was evoked after MDT, the antitumor effects in these groups remained poor due to the presence of large numbers of Tregs. Encouragingly, we found that the proportion of Tregs in the spleens and distant tumors of the mice injected with anti-CTLA4 was greatly reduced. Anti-CTLA4 has been approved by the FDA as an immune inhibitor and is currently applied in the clinical practice, and many studies have confirmed that its effects are better than those of PD-L1 in inhibiting the activity of immunosuppressive regulatory T cells (Tregs) and improving immunotherapy efficacy. The F/A@P+AMF+anti-CLTA4 group showed the lowest level of Tregs with corresponding increases in the CD8$^+$ CTL proportions in both the spleen and distant tumors of approximately 50% and 33.8%, respectively, which were much higher than those in the F@P+AMF (20.2%, 6.12%), F/A@P+AMF (23.4%, 10.4%) and F/A@P+anti-CTLA4 (16.3%, 17.8%) groups. Moreover, Teff proportions were significantly improved in the distant tumors of mice that received F/A@P+AMF+anti-CTLA4 as the primary tumor treatment (Fig. 6i). Overall, Fig. 6j shows that the F/A@P+AMF+anti-CTLA4 group induced the highest percentages of both the CD4$^+$ Teff/Treg and CD8$^+$ CTL/Treg ratios that are mainly responsible for cell immunity in antitumor immunotherapy. The T-cell correlation with the antitumor immune effect was prompted by the similar tendency of Treg inhibition, Teff activation and CTL amplification that plays a major role in the remodeling of the TIME.

Inducing long-term immune memory is essential for preventing disease recurrence because of the important ability of the immune system to recall pathogens for several decades [48]. Consequently, it is essential to assess the antitumor immune memory induced by this combination therapy. To evaluate the immune memory effect, we collected the spleens of the mice in the control group and combination treatment group at the end of the treatment cycle to evaluate memory CD8$^+$ T cells. Intriguingly, the percentage of T$_{EM}$ CD8$^+$ T cells (CD3$^+$CD8$^+$CD62 L-CD44$^+$) in the F/A@P+AMF+anti-CTLA4 group was substantially (nearly 5-fold) higher than that in the control group (Fig. 6g and h). Therefore, F/A@P+AMF+anti-CTLA4 treatment provided the greatest DC maturation, Treg inhibition, CTL infiltration, T$_{EM}$ CD8$^+$ T-cell activation, and tumor relapse prevention effects to reverse the immunosuppressive TME and enhance antitumor efficacy. This result clearly indicated that the
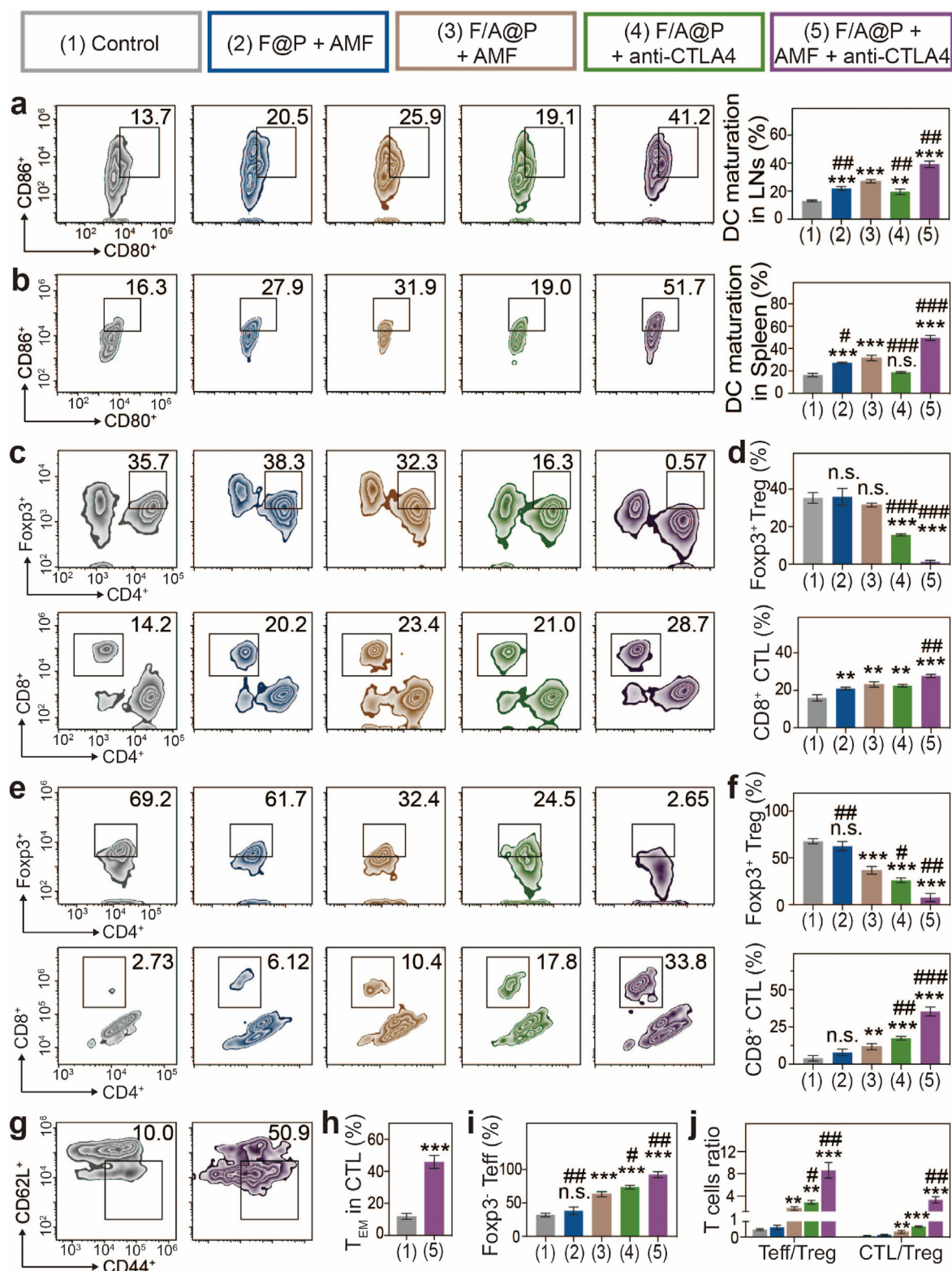
Fig. 6. Immune responses to combination therapy in an orthotopic bilateral 4T1 tumor-bearing mouse model. (a) FCM diagrams and quantification analysis of DC maturation in drain LNs adjacent to the primary tumors. (b) FCM diagrams and quantification analysis of DC maturation in spleens. (c) FCM diagrams and (d) quantification analysis of CTLs and Tregs in spleens. (e) FCM diagrams and (f) quantification analysis of CTLs and Tregs in distant tumors. (g) FCM diagrams and (h) quantification analysis of T$_{EM}$ cells in the mouse spleens of the control group and F/A@P + AMF + anti-CTLA4 group. (i) Proportions of Teff cells in secondary tumors based on (e) and (f). (j) Teff:Treg and CTL:Treg ratios in the secondary tumors. (The data are shown as the mean ± SD, n = 3 per group; n.s. represents no significance, *p < 0.05, **p < 0.01, ***p < 0.001 in comparison with the control group, #p < 0.05, ##p < 0.01, ###p < 0.001 in comparison with the F/A@P + AMF group).

strong antitumor immunity induced by the F/A@P-mediated thermal effect and ROS-generating platform can contribute to excellent therapeutic efficacy and antimetastatic ability in a TNBC mouse model.

In addition, we used western blotting to detect HSP70 expression in primary tumors to assess ICD levels in vivo. The immunoblot results shown in Fig. 7a indicate that the HSP70 expression level in F/A@P-treated mice was much higher than those in the other groups. This finding indicated that magnetothermal therapy triggered synergistic ICD effects through evoked DAMPs such as HSP70. As shown in Fig. 7c, the H&E-stained tumor slices displayed nearly full fields of deformed nuclei and apoptotic areas in the F/A@P+AMF+anti-CTLA4 group, which was similar to the results of the TUNEL assay. Ki-67 analysis revealed few detectable histopathological abnormalities and almost no proliferation. Moreover, we found that the cytotoxic CD8$^+$ T cells in the F/A@P+AMF+anti-CTLA4 group showed significant proliferation in distant tumors. ELISA showed that the mice in the F/A@P +AMF+anti-

CTLA4 group had the highest expression levels of antitumor cytokines, such as TNF-α, interferon (IFN)-γ, IL-6 and IL-12 (Fig. 7b). All of these cytokines are antitumor inflammatory factors secreted by immune cells after triggering a strong immune response, further proving that the F/A@P-mediated thermal effect and ROS dual-induced ICD effectively reversed the poor immunogenicity and further cooperated with ICB to amplify the antitumor systemic immune response to inhibit distant tumors. Finally, we found that the serum biochemical markers of the mice receiving F/A@P treatment were within the normal ranges, and there was almost no histopathological damage to the major organs. Thus, systemic toxicity of the F/A@P gels in mice was negligible, preventing the side effects and disadvantages of traditional treatments (Figs. S15 and 16). The above results suggest the remarkable therapeutic efficacy, excellent biological safety and potential clinical application of F/A@P gels.
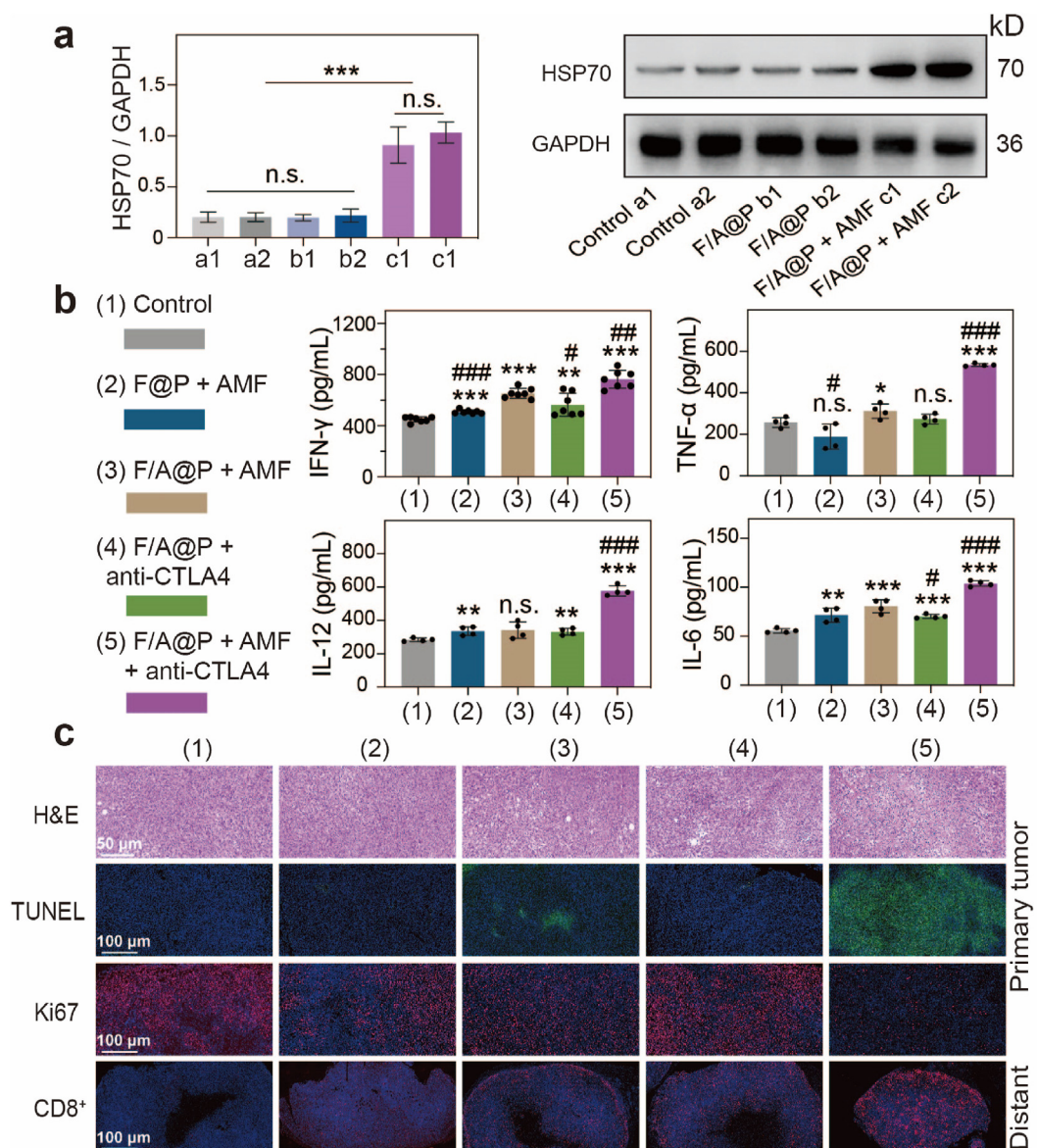

Fig. 7. In vivo synergistic therapy of tumors. (a) The expression of HSP70 in primary tumors was detected by western blotting, and corresponding quantification analysis was carried out for 2 mice in each group. (b) The levels of TNF-α, IFN-γ, IL-6 and IL-12 in the serum of mice were measured by ELISA. (c) H&E, TUNEL and Ki-67 immunochemical staining images of the primary tumor, and CD8$^+$ T-cell immunochemical staining of the distant tumor. (Scale bars: 50 μm, 100 μm). (The data are shown as the mean ± SD, n = 3 per group; n.s. represents no significance, *p < 0.05, **p < 0.01, ***p < 0.001 in comparison with the control group, #p < 0.05, ##p < 0.01, ###p < 0.001 in comparison with the F/A@P + AMF group).

4. Conclusion

In this study, we proposed a unique magnetothermal dynamic immunotherapy strategy based on liquid-solid transformation porous versatile implants to enhance anti-malignant cancer efficacy. The constructed F/A@P produced oxygen-independent free radicals under AMF actuation, not only directly eliminating cancer cells in hypoxic tumors but also inducing large-scale ICD by magnetothermal effects and endogenous oxidative stress accumulation, thus enhancing tumor immunogenicity that when combined with CTLA4 blockade promotes an efficient immunotherapy response to achieve highly effective cancer immunotherapy. This combination strategy showed great antitumor efficacy in treating artificial spontaneous metastasis orthotopic bilateral TNBC in tumor models, not only eliminating primary tumors and attacking and killing distant spreading metastatic tumors but also offering strong immune protection, including increased DC maturation, T-cell infiltration and memory T-cell activation, and inhibited Treg T-cell function to prevent tumor relapse. In conclusion, our study presents dynamic magnetocaloric immunotherapy based on injectable F/A@P gels for the minimally invasive treatment of TNBC, reversing the immunosuppressive TME and enhancing antitumor efficacy. Considering that all components in our controllable oxygen-irrelevant free radical generators are FDA-approved and the extensive attention attracted by magnetocaloric therapy and its application prospects, our research may indeed have great potential for further clinical translation.

CRediT author statement

Mengna Wang: Investigation, Methodology, Writing-Original Draft. Siyu Deng: Formal analysis. Yijia Cao: Formal analysis. Hang Zhou: Methodology. Wei Wei: Methodology. Kexiao Yu: Writing-Review & Editing, Funding acquisition. Youde Cao: Resources, Project administration. Bing Liang: Term, Conceptualization, Funding acquisition, Project administration.

Ethics statement

All animal procedures were performed in accordance with the Guidelines of the Ministry of Science and Technology of Health Guide for Care and Use of Laboratory Animals, China and were approved by the institutional ethics committee (IEC) of Chongqing Medical University.

Declaration of competing interest

The authors declare that they have no known competing financial interests or personal relationships that could have appeared to influence the work reported in this paper.

Data availability

No data was used for the research described in the article.

Appendix A. Supplementary data

Supplementary data to this article can be found online at https://doi.org/10.1016/j.mtbio.2022.100442.

References

[1] Y. Yang, Cancer immunotherapy: harnessing the immune system to battle cancer, J. Clin. Invest. 125 (9) (2015) 3335–3337, https://doi.org/10.1172/jci83871.

[2] Z. Xu, S. Zeng, Z. Gong, Y. Yan, Exosome-based immunotherapy: a promising approach for cancer treatment, Mol. Cancer 19 (1) (2020) 160, https://doi.org/10.1186/s12943-020-01278-3.

[3] S.P. Kurup, N.S. Butler, J.T. Harty, T cell-mediated immunity to malaria, Nat. Rev. Immunol. 19 (7) (2019) 457–471, https://doi.org/10.1038/s41577-019-0158-z.

[4] D.M. Pardoll, The blockade of immune checkpoints in cancer immunotherapy, Nat. Rev. Cancer 12 (4) (2012) 252–264, https://doi.org/10.1038/nrc3239.

[5] A. Azad, S. Yin Lim, Z. D'Costa, K. Jones, A. Diana, O.J. Sansom, P. Kruger, S. Liu, W.G. McKenna, O. Dushek, R.J. Muschel, E. Fokas, PD-L1 blockade enhances response of pancreatic ductal adenocarcinoma to radiotherapy, EMBO Mol. Med. 9 (2) (2017) 167–180, https://doi.org/10.15252/emmm.201606674.

[6] S. Upadhaya, S.T. Neftelino, J.P. Hodge, C. Oliva, J.R. Campbell, J.X. Yu, Combinations take centre stage in PD1/PDL1 inhibitor clinical trials, Nat. Rev. Drug Discov. 20 (3) (2021) 168–169, https://doi.org/10.1038/d41573-020-00204-y.

[7] N. Harbeck, M. Gnant, Breast cancer, Lancet 389 (10074) (2017) 1134–1150, https://doi.org/10.1016/s0140-6736(16)31891-8.

[8] E. Vagia, D. Mahalingam, M. Cristofanilli, The landscape of targeted therapies in TNBC, Cancers (Basel) 12 (4) (2020), https://doi.org/10.3390/cancers12040916.

[9] G. Kroemer, L. Galluzzi, O. Kepp, L. Zitvogel, Immunogenic cell death in cancer therapy, Annu. Rev. Immunol. 31 (2013) 51–72, https://doi.org/10.1146/annurev-immunol-032712-100008.

[10] Z. Li, X. Lai, S. Fu, L. Ren, H. Cai, H. Zhang, Z. Gu, X. Ma, K. Luo, Immunogenic cell death activates the tumor immune microenvironment to boost the immunotherapy efficiency, Adv. Sci. (Weinh) (2022), e2201734, https://doi.org/10.1002/advs.202201734.

[11] S. Zhang, J. Wang, Z. Kong, X. Sun, Z. He, B. Sun, C. Luo, J. Sun, Emerging photodynamic nanotherapeutics for inducing immunogenic cell death and potentiating cancer immunotherapy, Biomaterials 282 (2022), 121433, https://doi.org/10.1016/j.biomaterials.2022.121433.

[12] T. Xu, Y. Ma, Q. Yuan, H. Hu, X. Hu, Z. Qian, J.K. Rolle, Y. Gu, S. Li, Enhanced ferroptosis by oxygen-boosted phototherapy based on a 2-in-1 nanoplatform of ferrous hemoglobin for tumor synergistic therapy, ACS Nano 14 (3) (2020) 3414–3425, https://doi.org/10.1021/acsnano.9b09426.

[13] H. Zhao, J. Xu, Y. Wang, C. Sun, L. Bao, Y. Zhao, X. Yang, Y. Zhao, A photosensitizer discretely loaded nanoaggregate with robust photodynamic effect for local treatment triggers systemic antitumor responses, ACS Nano 16 (2) (2022) 3070–3080, https://doi.org/10.1021/acsnano.1c10590.

[14] X. Wang, Y. Mao, C. Sun, Q. Zhao, Y. Gao, S. Wang, A versatile gas-generator promoting drug release and oxygen replenishment for amplifying photodynamic-chemotherapy synergetic anti-tumor effects, Biomaterials 276 (2021), 120985, https://doi.org/10.1016/j.biomaterials.2021.120985.

[15] K.W. Lee, Y. Wan, X. Li, X. Cui, S. Li, C.S. Lee, Recent progress of alkyl radicals generation-based agents for biomedical applications, Adv. Healthc. Mater. 10 (10) (2021), e2100055, https://doi.org/10.1002/adhm.202100055.

[16] J.A. Milligan, J.P. Phelan, S.O. Badir, G.A. Molander, Alkyl carbon-carbon bond formation by nickel/photoredox cross-coupling, Angew Chem. Int. Ed. Engl. 58 (19) (2019) 6152–6163, https://doi.org/10.1002/anie.201809431.

[17] X. Li, S. Lee, J. Yoon, Supramolecular photosensitizers rejuvenate photodynamic therapy, Chem. Soc. Rev. 47 (4) (2018) 1174–1188, https://doi.org/10.1039/c7cs00594f.

[18] B. Liang, B. Qiao, K. Yu, J. Cao, H. Zhou, Q. Jiang, Y. Zhong, Y. Cao, Z. Wang, Y. Zheng, Mitochondrial glutathione depletion nanoshuttles for oxygen-irrelevant free radicals generation: a cascaded hierarchical targeting and theranostic strategy against hypoxic tumor, ACS Appl. Mater. Interfaces 14 (11) (2022) 13038–13055, https://doi.org/10.1021/acsami.1c24708.

[19] H. Gavilán, S.K. Avugadda, T. Fernández-Cabada, N. Soni, M. Cassani, B.T. Mai, R. Chantrell, T. Pellegrino, Magnetic nanoparticles and clusters for magnetic hyperthermia: optimizing their heat performance and developing combinatorial therapies to tackle cancer, Chem. Soc. Rev. 50 (20) (2021) 11614–11667, https://doi.org/10.1039/d1cs00427a.

[20] M. Chang, Z. Hou, M. Wang, C. Li, J. Lin, Recent advances in hyperthermia therapy-based synergistic immunotherapy, Adv. Mater. 33 (4) (2021), e2004788, https://doi.org/10.1002/adma.202004788.

[21] J. Pan, Y. Xu, Q. Wu, P. Hu, J. Shi, Mild magnetic hyperthermia-activated innate immunity for liver cancer therapy, J. Am. Chem. Soc. 143 (21) (2021) 8116–8128, https://doi.org/10.1021/jacs.1c02537.

[22] L. Galluzzi, T. Yamazaki, G. Kroemer, Linking cellular stress responses to systemic homeostasis, Nat. Rev. Mol. Cell Biol. 19 (11) (2018) 731–745, https://doi.org/10.1038/s41580-018-0068-0.

[23] B. Liu, C. Li, G. Chen, B. Liu, X. Deng, Y. Wei, J. Xia, B. Xing, P. Ma, J. Lin, Synthesis and optimization of MoS(2)@Fe(3)O(4)-ICG/Pt(IV) nanoflowers for MR/IR/PA bioimaging and combined PTT/PDT/chemotherapy triggered by 808 nm laser, Adv. Sci. (Weinh) 4 (8) (2017), 1600540, https://doi.org/10.1002/advs.201600540.

[24] C.I. Nkanga, A. Fisch, M. Rad-Malekshahi, M.D. Romic, B. Kittel, T. Ullrich, J. Wang, R.W.M. Krause, S. Adler, T. Lammers, W.E. Hennink, F. Ramazani, Clinically established biodegradable long acting injectables: an industry perspective, Adv. Drug Deliv. Rev. 167 (2020) 19–46, https://doi.org/10.1016/j.addr.2020.11.008.

[25] B. Pelaz, C. Alexiou, R.A. Alvarez-Puebla, F. Alves, A.M. Andrews, S. Ashraf, L.P. Balogh, L. Ballerini, A. Bestetti, C. Brendel, S. Bosi, M. Carril, W.C. Chan, C. Chen, X. Chen, X. Chen, Z. Cheng, D. Cui, J. Du, C. Dullin, A. Escudero, N. Feliu, M. Gao, M. George, Y. Gogotsi, A. Grünweller, Z. Gu, N.J. Halas, N. Hampp, R.K. Hartmann, M.C. Hersam, P. Hunziker, J. Jian, X. Jiang, P. Jungebluth, P. Kadhiresan, K. Kataoka, A. Khademhosseini, J. Kopeček, N.A. Kotov, H.F. Krug, D.S. Lee, C.M. Lehr, K.W. Leong, X.J. Liang, M. Ling Lim, L.M. Liz-Marzán, X. Ma, P. Macchiarini, H. Meng, H. Möhwald, P. Mulvaney, A.E. Nel, S. Nie, P. Nordlander, T. Okano, J. Oliveira, T.H. Park, R.M. Penner, M. Prato, V. Puntes, V.M. Rotello, A. Samarakoon, R.E. Schaak, Y. Shen, S. Sjöqvist, A.G. Skirtach, M.G. Soliman, M.M. Stevens, H.W. Sung, B.Z. Tang, R. Tietze, B.N. Udugama, J.S. VanEpps, T. Weil, P.S. Weiss, I. Willner, Y. Wu, L. Yang, Z. Yue, Q. Zhang, Q. Zhang, X.E. Zhang, Y. Zhao, X. Zhou, W.J. Parak, Diverse applications of nanomedicine, ACS Nano 11 (3) (2017) 2313–2381, https://doi.org/10.1021/acsnano.6b06040.
[26] D.R. Green, T. Ferguson, L. Zitvogel, G. Kroemer, Immunogenic and tolerogenic cell death, Nat. Rev. Immunol. 9 (5) (2009) 353–363, https://doi.org/10.1038/nri2545.
[27] J.D. Hayes, A.T. Dinkova-Kostova, K.D. Tew, Oxidative stress in cancer, Cancer Cell 38 (2) (2020) 167–197, https://doi.org/10.1016/j.ccell.2020.06.001.
[28] Y. Liu, P. Bhattarai, Z. Dai, X. Chen, Photothermal therapy and photoacoustic imaging via nanotheranostics in fighting cancer, Chem. Soc. Rev. 48 (7) (2019) 2053–2108, https://doi.org/10.1039/c8cs00618k.
[29] G. Morad, B.A. Helmink, P. Sharma, J.A. Wargo, Hallmarks of response, resistance, and toxicity to immune checkpoint blockade, Cell 184 (21) (2021) 5309–5337, https://doi.org/10.1016/j.cell.2021.09.020.
[30] T.K. Kim, E.N. Vandsemb, R.S. Herbst, L. Chen, Adaptive immune resistance at the tumour site: mechanisms and therapeutic opportunities, Nat. Rev. Drug Discov. 21 (7) (2022) 529–540, https://doi.org/10.1038/s41573-022-00493-5.
[31] C. Twyman-Saint Victor, A.J. Rech, A. Maity, R. Rengan, K.E. Pauken, E. Stelekati, J.L. Benci, B. Xu, H. Dada, P.M. Odorizzi, R.S. Herati, K.D. Mansfield, D. Patsch, R.K. Amaravadi, L.M. Schuchter, H. Ishwaran, R. Mick, D.A. Pryma, X. Xu, M.D. Feldman, T.C. Gangadhar, S.M. Hahn, E.J. Wherry, R.H. Vonderheide, A.J. Minn, Radiation and dual checkpoint blockade activate non-redundant immune mechanisms in cancer, Nature 520 (7547) (2015) 373–377, https://doi.org/10.1038/nature14292.
[32] H. Zhou, K. Yu, H. Jiang, R. Deng, L. Chu, Y. Cao, Y. Zheng, W. Lu, Z. Deng, B. Liang, A three-in-one strategy: injectable biomimetic porous hydrogels for accelerating bone regeneration via shape-adaptable Scaffolds, controllable magnesium ion release, and enhanced osteogenic differentiation, Biomacromolecules 22 (11) (2021) 4552–4568, https://doi.org/10.1021/acs.biomac.1c00842.
[33] Y. Zhang, S. Tian, L. Huang, Y. Li, Y. Lu, H. Li, G. Chen, F. Meng, G.L. Liu, X. Yang, J. Tu, C. Sun, L. Luo, Reactive oxygen species-responsive and Raman-traceable hydrogel combining photodynamic and immune therapy for postsurgical cancer treatment, Nat. Commun. 13 (1) (2022) 4553, https://doi.org/10.1038/s41467-022-32160-z.
[34] J.Q. Zhu, H. Wu, Z.L. Li, X.F. Xu, H. Xing, M.D. Wang, H.D. Jia, L. Liang, C. Li, L.Y. Sun, Y.G. Wang, F. Shen, D.S. Huang, T. Yang, Responsive hydrogels based on

triggered click reactions for liver cancer, Adv. Mater. (2022), e2201651, https://doi.org/10.1002/adma.202201651.
[35] A.P. King, J.J. Wilson, Endoplasmic reticulum stress: an arising target for metal-based anticancer agents, Chem. Soc. Rev. 49 (22) (2020) 8113–8136, https://doi.org/10.1039/d0cs00259c.
[36] J.R. Cubillos-Ruiz, S.E. Bettigole, L.H. Glimcher, Tumorigenic and immunosuppressive effects of endoplasmic reticulum stress in cancer, Cell 168 (4) (2017) 692–706, https://doi.org/10.1016/j.cell.2016.12.004.
[37] A.D. Garg, A. Kaczmarek, O. Krysko, P. Vandenabeele, D.V. Krysko, P. Agostinis, ER stress-induced inflammation: does it aid or impede disease progression? Trends Mol. Med. 18 (10) (2012) 589–598, https://doi.org/10.1016/j.molmed.2012.06.010.
[38] N. Yatim, S. Cullen, M.L. Albert, Dying cells actively regulate adaptive immune responses, Nat. Rev. Immunol. 17 (4) (2017) 262–275, https://doi.org/10.1038/nri.2017.9.
[39] D.V. Krysko, A.D. Garg, A. Kaczmarek, O. Krysko, P. Agostinis, P. Vandenabeele, Immunogenic cell death and DAMPs in cancer therapy, Nat. Rev. Cancer 12 (12) (2012) 860–875, https://doi.org/10.1038/nrc3380.
[40] T. Gong, L. Liu, W. Jiang, R. Zhou, DAMP-sensing receptors in sterile inflammation and inflammatory diseases, Nat. Rev. Immunol. 20 (2) (2020) 95–112, https://doi.org/10.1038/s41577-019-0215-7.
[41] S.C. Eisenbarth, Dendritic cell subsets in T cell programming: location dictates function, Nat. Rev. Immunol. 19 (2) (2019) 89–103, https://doi.org/10.1038/s41577-018-0088-1.
[42] X. Yin, S. Chen, S.C. Eisenbarth, Dendritic cell regulation of T helper cells, Annu. Rev. Immunol. 39 (2021) 759–790, https://doi.org/10.1146/annurev-immunol-101819-025146.
[43] A.J. Korman, S.C. Garrett-Thomson, N. Lonberg, The foundations of immune checkpoint blockade and the ipilimumab approval decennial, Nat. Rev. Drug Discov. 21 (7) (2022) 509–528, https://doi.org/10.1038/s41573-021-00345-8.
[44] C.F. Friedman, T.A. Proverbs-Singh, M.A. Postow, Treatment of the immune-related adverse effects of immune checkpoint inhibitors: a review, JAMA Oncol. 2 (10) (2016) 1346–1353, https://doi.org/10.1001/jamaoncol.2016.1051.
[45] D.E. Speiser, P.C. Ho, G. Verdeil, Regulatory circuits of T cell function in cancer, Nat. Rev. Immunol. 16 (10) (2016) 599–611, https://doi.org/10.1038/nri.2016.80.
[46] R.J. Kishton, M. Sukumar, N.P. Restifo, Metabolic regulation of T cell longevity and function in tumor immunotherapy, Cell Metabol. 26 (1) (2017) 94–109, https://doi.org/10.1016/j.cmet.2017.06.016.
[47] M. Ruterbusch, K.B. Pruner, L. Shehata, M. Pepper, In vivo CD4(+) T cell differentiation and function: revisiting the Th1/Th2 paradigm, Annu. Rev. Immunol. 38 (2020) 705–725, https://doi.org/10.1146/annurev-immunol-103019-085803.
[48] A. Byrne, P. Savas, S. Sant, R. Li, B. Virassamy, S.J. Luen, P.A. Beavis, L.K. Mackay, P.J. Neeson, S. Loi, Tissue-resident memory T cells in breast cancer control and immunotherapy responses, Nat. Rev. Clin. Oncol. 17 (6) (2020) 341–348, https://doi.org/10.1038/s41571-020-0333-y.